NANO: Brief Reports and Reviews
Vol. 2, No. 5 (2007) 249–271
© World Scientific Publishing Company
World Scientific
www.worldscientific.com

EXPERIMENTAL NANOMECHANICS OF ONE-DIMENSIONAL NANOMATERIALS BY *IN SITU* MICROSCOPY

XIAODONG HAN* and ZE ZHANG†
Institute of Microstructure and Property of Advanced Materials
Beijing University of Technology, 100022 Beijing, P. R. China
**xdhan@bjut.edu.cn*
†zezhang@bjut.edu.cn

ZHONG LIN WANG
School of Materials Science and Engineering
Georgia Institute of Technology, Atlanta, GA 30332, USA
zhong.wang@mse.gatech.edu

Received 9 August 2007
Revised 21 September 2007

This paper provides a comprehensive review on the methodological development and technical applications of *in situ* microscopy, including transmission electron microscopy (TEM), scanning electron microscopy (SEM) and atomic force microscopy (AFM), developed in the last decade for investigating the structure-mechanical-property relationship of a single one-dimensional nanomaterial, such as nanotube, nanowire and nanobelt. The paper covers both the fundamental methods and detailed applications, including AFM-based static elastic and plastic measurements of a carbon nanotube, external field-induced resonance dynamic measurement of elastic modulus of a nanotube/nanowire, nano-indentation, and *in situ* plastic deformation process of a nanowire. Details are presented on the elastic property measurements and direct imaging of plastic to superplastic behavior of semiconductor nanowires at atomic resolution, providing quantitative information on the mechanical behavior of nanomaterials. The studies on the Si and SiC nanowires clearly demonstrated their distinct, "unexpected" and superior plastic mechanical properties. Finally, a perspective is given on the future of nanomechanics.

Keywords: Nanomechanics; *in situ* TEM; atomic force microscopy; elastic modulus; superplasticity.

1. Introduction

One-dimensional (1D) nanomaterials such as nanotubes (NTs),[1] nanowires (NWs) and nanobelts (NBs) are building blocks for bottom-up nanotechnology.[2] The well-defined chemical and crystallographic structure, morphologies and architectures, and predictable electronic properties as well as the composition and functional varieties make the NWs and NBs the ideal candidates for bottom-up nanotechnology, for constructing various complex nanodevices. Individual NWs and NBs are also excellent functional materials for field emission effects, laser emitting, optoelectronics, electronics, energy harvesting, etc. Many single NWs, NBs and nanotubes exhibit unusual properties. As far as mechanical properties are concerned,

the known properties include ultra-high strength of carbon tubes,[3–5] high strength, high hardness and toughness of SiC nanowires,[6] low temperature plasticity and superplasticity[7–9] of covalence-bonded NWs and ultra high strength of Au and Ag nanowires.[10,11] Under stress or strain, the structure and physical properties of nanowires and nanotubes change dramatically with possible band energy shift.[12] It was revealed that under stress, single-walled carbon nanotubes can be tuned from isolators to semiconductors to metallic conductors.[13,14] Si nanowires show great pizeo-electric effect with deformation.[14]

Numerous methods and techniques have been developed to measure the strength of the nanowires, nanotubes and nanobelts in the elastic range.[3,6,12] Efforts were also made to interpret the elastoplastic transitions in the nanowires and ultra-high strength of the NWs, NTs, etc. using AFM bending tests and nano-indentation. However, the interpretation of the elastoplastic transition heavily relied on the computer simulations. The dislocation initiation, propagation and reaction can only be imagined in the case of deforming NWs, for example in the super-high strength Au NW deformations.[10] So far, there were only a few direct atomic scale experimental evidences revealing the elastic–plastic transformations in covalence-bonded NWs.[7–9] This is in contrast to the well-developed mechanical deformation and strength theories in bulk materials.[15] There is no clear understanding on many peculiar phenomena of the unusual mechanical properties of one-dimensional nanomaterial. It is urgently necessary to develop methods, techniques and tools to conduct investigations to provide experimental results and evidences on the one-dimensional nanomaterials.

In this paper, we review the methods and technologies that have been developed in the last decades for quantifying the mechanical properties of 1D nanomaterials-based *in situ* microscopy, including atomic force microscopy (AFM), *in situ* scanning electron microscopy (SEM) and transmission electron microscopy (TEM). Integrating these electron microscopy techniques, i.e., combining the high resolution imaging systems with deformation abilities such as AFM, SPM, electron heating and other means, the advantages offered by *in situ* electron microscopy can be further developed. For example, TEM-deformation hybrid system can provide a direct imaging on the deformation process at atomic resolution or close with simultaneous chemical composition, electronic and crystallographic structure as well as defect evolution process, so that one is able to directly correlate the measured mechanical properties with the microstructure of the measured object. A better understanding will be provided for capturing the insight of the mechanical behavior at nanoscale.

2. Elastic Nanomechanics by Scanning Probe Microscopy

Among the various techniques, scanning probe microscopy (STM, AFM) has been a major tool in investigating the properties of individual nanostructures. STM is a conjunction use of atomic scale imaging with atomic resolution spectroscopy, and it is an ideal approach for detecting local electronic structure. AFM is powerful in probing the mechanical behavior at nanoscale. This section will describe the investigation of mechanical properties of one-dimensional nanomaterials by AFM.

2.1. *Elastic modulus of multi-walled carbon nanotube*

AFM tip-based manipulation technique is one of the most powerful approaches for probing the elastic properties of carbon nanotubes.[6] The carbon nanotubes were first scattered and dispersed on a flat MoS_2 (low coefficient of friction) substrate surface, then a metal mesh was placed onto the substrate followed by deposition of SiO_2 to form squared pads on the substrate. The deposited SiO_2 pads were used to fix the nanowires and nanotubes on the substrate. After the deposition, the metal mesh was removed from the substrate. By examining the entire substrate, some of the nanotubes or nanowires with parts of their lengths were hold by the SiO_2 pads, forming an one-end fixed stationary beam. Using the tip of an AFM to deflect the nanotube, the displacement of the nanotube can be directly related to the force reflected on the tip. Figure 1 shows the force-displacement f–δ curve measured as a function of the distance from the fixed point (a) and the corresponding force constant. The solid line is a $1/a^3$ fitting of the experimentally obtained curve. For the multi-walled nanotubes studied, the bending modulus is determined to be close to 1 TPa which is close to the values measured by other means.

This type of measurement is based on several assumptions. First, one-end of the nanotube

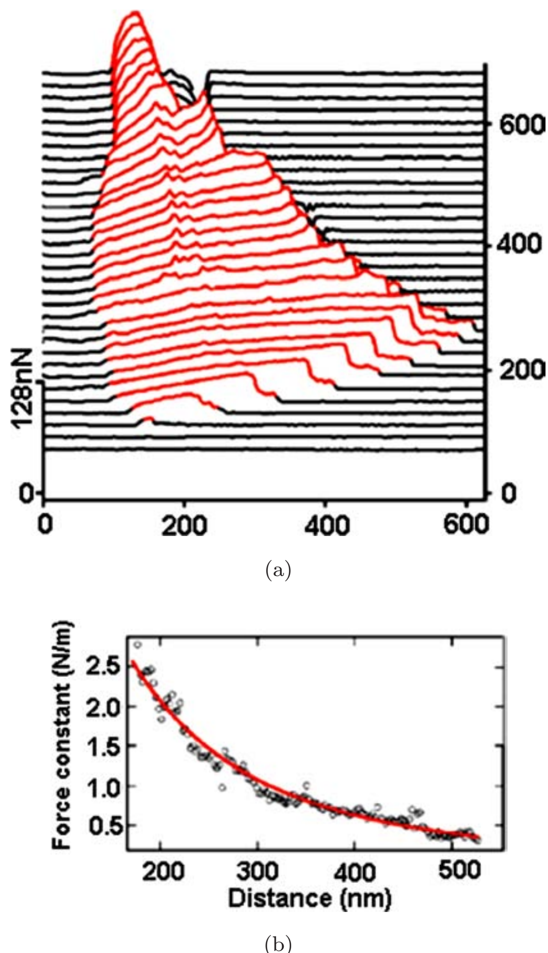

Fig. 1. (a) Surface plot showing the F–d response of a 32.9-nm-diameter MWNT recorded with a normal load of 16.4 nN. The image is tilted 30° and displays only 30 of the ∼300 F–d traces in the original image for clarity. The nanotube is pinned by a SiO pad beyond the top of the image. The data were recorded in water to minimize the nanotube-MoS_2 friction force. (b) Dependence of force constant on position x along the axis of the same nanotube. The carbon nanotubes used in these studies were purified by oxidation to 5% of the initial sample (from Ref. 6).

is well-affixed and it cannot move or be loose during the deflection driven by the AFM tip. The tip is believed to be "perfectly" solid and stiff and there is no deformation of the tip during the deflection. This assumption could be challenged eventually because the studied nanowires or tubes may be stronger than the material making of the tip and therefore the tip must be carefully selected. Finally, no sliding is permitted between the tip and the nanotube. An alternative technique has been developed by Salvetat *et al.*[16] and it can be used as a "bending-bridge" for measuring the Young's modulus by the AFM tip. In this configuration, the displacement at the middle of the bridge is directly proportional to

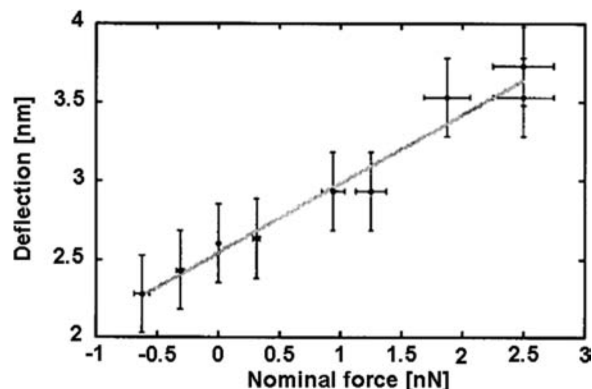

Fig. 2. Deflection versus the applied force f for an arc-discharge-produced MWNT. The suspended length was $L = 350$ nm, and the diameter of the tube was 10 nm. The solid line is a linear regression fit of the experimental data, with a slope inversely proportional to the Young's modulus (from Ref. 16).

the applied[17] force by:

$$\delta = \frac{fL^3}{\alpha EI}, \tag{1}$$

where $\alpha = 192$ for a clamped beam and 48 for a simple supported beam. Considering the difficulty in calibrating the absolute force and the deflection of the beam, the change in deflection as a function of the change in load is measured, and the curve displayed in Fig. 2 is a linear curve whose slope gives the elastic modulus of the nanotube if the suspended length L and the inner and outer diameters of the nanotubes were known. For the nanotube from which the data in Fig. 2 were recorded, its elastic modulus was measured to be about 1.1 TPa with an error of -20 to $+50\%$.

2.2. *Elastic behavior of aligned 1D nanomaterial's array*

For the aligned NWs, we have recently demonstrated an AFM-based technique for measuring the elastic properties of individual ZnO NW without destructing the specimen.[18,19] By simultaneously recording the topography and lateral force image in AFM contact mode when the AFM tip scans across the aligned nanowire arrays, the elastic modulus of individual NWs is determined. This technique allows a measurement of the mechanical properties of individual NWs of different lengths in an aligned array without destructing or manipulating the sample.

The principle for the AFM measurement is illustrated in Fig. 3. In AFM contact mode, a

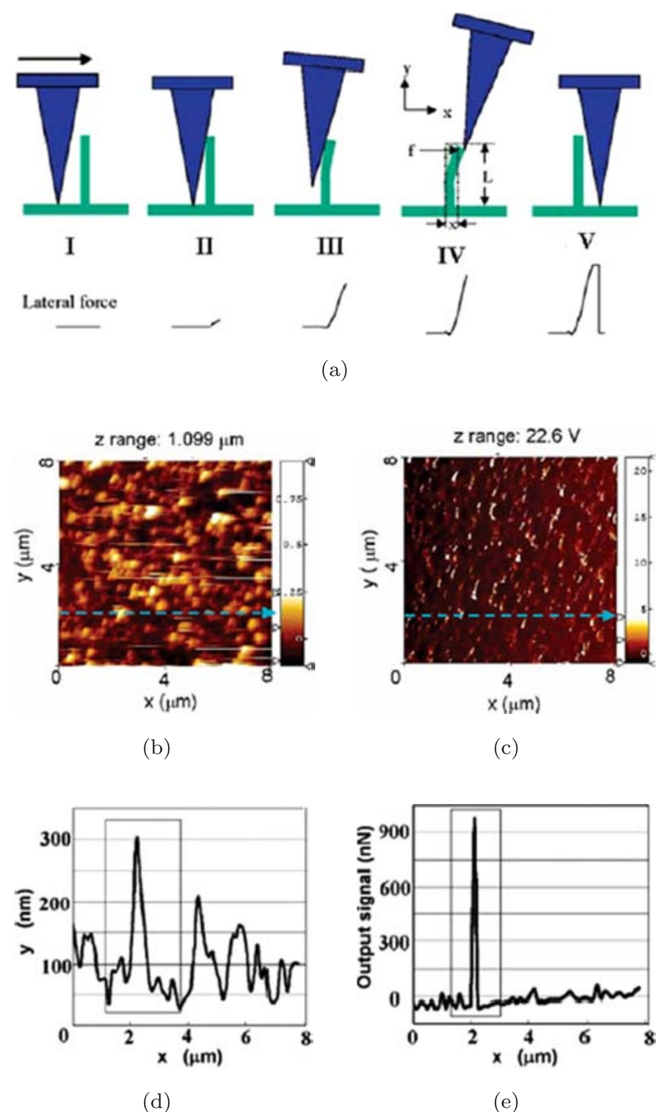

Fig. 3. (a) Procedures for measuring the elastic modulus of a nanowire in the AFM contacting mode; (b) topography image and (c) lateral force image of the aligned ZnO nanowire arrays received in AFM contacting mode. The elastic modulus of each nanowire in the scanning range can be derived from these images. (d) and (e) Line profiles along the dashed lines in (b) and (c) showing the curves of scanner retracting distance versus the nanowire lateral displacement and the lateral force versus the lateral displacement, respectively (from Ref. 18).

constant normal force is kept between the tip and sample surface. The tip scans over the top of the ZnO NW and the tip's height is adjusted according to the surface morphology and local contacting force. Before the tip meets a NW, a small lateral force is observed (Fig. 3(a-I)). When the tip comes in contact with a NW, the lateral force increases almost linearly as the NW is elastically bent from its equilibrium position (Fig. 3(a-III)). At the largest bending position, as illustrated in Fig. 3, the tip crosses the top of the NW, then the NW is released; the lateral force drops suddenly and reaches the ordinary level (Fig. 3(a-V)).

The elastic modulus is derived based on the following calculation. From the geometrical relationship illustrated in Fig. 3(a-IV), when a vertical NW experiences a lateral force f parallel to the scanning direction, the force f can be expressed as:

$$f = 3EI\frac{x}{L^3}, \tag{2}$$

where E and I are the elastic modulus and momentum of inertia of the NW, x is the lateral displacement perpendicular to the NW, and L is the length of the NW. From Hook's law, the spring constant is $K = f/x$. For a ZnO NW with a hexagonal cross-section, its momentum of inertia is $I = (5(3^{1/2})/16)a^4$, where a is the radius of the NW. Therefore, the elastic modulus is given by:

$$E = \frac{16L^3K}{15\sqrt{3}a^4}. \tag{3}$$

The displacement and the lateral force were determined from the topography image and the corresponding lateral force image, as shown in Figs. 3(b) and 3(c), respectively. To ensure that the center of the conical tip touches the center of the NW as assumed in theoretical calculation, both curves were read from the center of the NW as indicated in the images by dashed lines. Taking a line scan across the middle point of a spot in the topography image, a curve for the scanner retracting distance versus the NW lateral displacement was obtained, as shown in Fig. 3(d). Likewise, the maximum maximal lateral force for bending the NW was measured by acquiring a scanning profile at the corresponding line in the lateral force image (as indicated in Fig. 3(e)). Combining the measured x_m and f_m from the two line profiles, the spring constant $K = f_m/x_m$ was obtained. For the ZnO nanowires grown on sapphire surfaces with an average diameter of 45 nm, the elastic modulus was determined to be 29 ± 8 GPa. This technique provided a direct observation on the mechanical properties of aligned NWs, which is of great importance for their applications in electronics, optoelectronics, sensors, and actuators.

2.3. *Elastic behavior of nanobelts*

One of the most important strategies is deforming a NB that is supported at the two ends using an

AFM tip, which pushes the NB at its middle point. Quantifying the middle-point force-displacement curve gives the elastic modulus. The accuracy of this measurement is, however, limited by the size of the tip and the accuracy of positioning the AFM tip right at the middle of the 1D nanostructure due to the unavoidable hysteresis of the piezoceramic actuator of the AFM cantilever. We have demonstrated a new approach for quantifying the elastic deformation behavior of a NW by fitting the image profile measured using atomic force microscopy (AFM) in contact mode along the entire length of a bridged/suspended NB/NW/nanotube under different load forces (Figs. 4(a)–4(c)).[19]

The profile images of the NB recorded the deformation of all of the points along its length under different applied forces (Fig. 4(b)). One profile could contain up to 650 points, and each point on the suspended portion of NB in the images can be regarded as a mechanical measurement. Consistently fitting the measured deformation profiles can uniquely determine if the measured data are best fit by either the clamped-clamped beam model (CCBM) or the free-free beam model (FFBM) without pre-assumption (Fig. 4(c)), and it eliminates the uncertainty in defining the central point of the suspended beam, thus, greatly increased the precision and reliability of the measurement for elastic modulus.

2.4. *Nano-indentation*

Nano-indentation is one of the most applicable tools at present time to extract mechanical properties of materials at nanoscale (normally nanodomains) to provide information on localized elastic and plastic deformation zones.[20] Nano-indentation has been widely used for mechanical property characterization of nanograin structured bulk materials[21] and thin films,[22] and has been successful in combining experimental measurements with simulations.[23] Recently, integrated with atomic force microscope,[24,25] nano-indentation has been successfully applied in featuring the mechanical properties of one-dimensional nanomaterials. Quantified displacement versus force functions can be fully mapped together with the high spatial resolution nanoscale imaging of the tested nanomaterials prior to and post testing. The elastic modulus, hardness and plastic deformation characters of the indented materials can be provided simultaneously over a large surface area.[24]

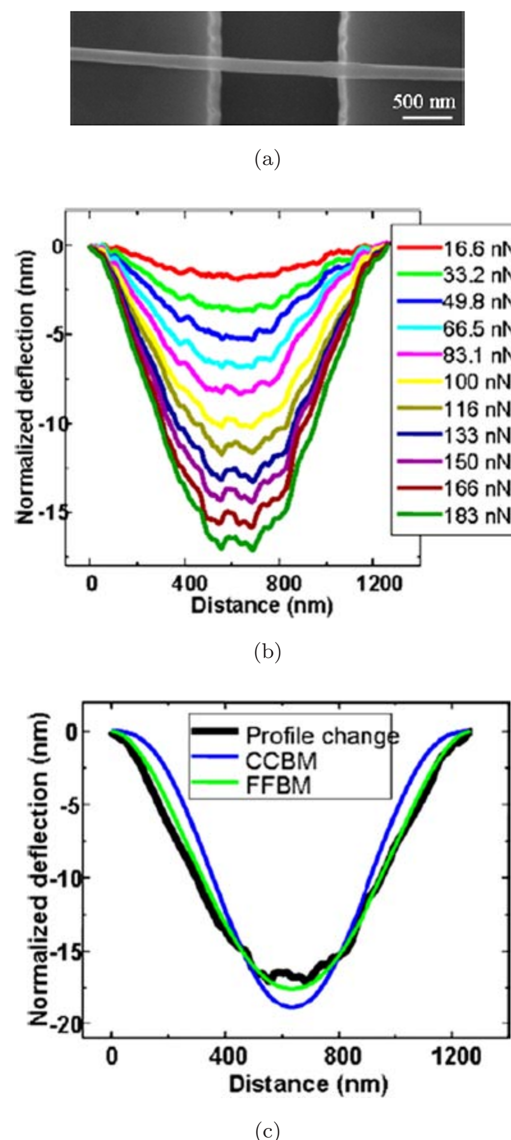

Fig. 4. (a) SEM image of one NB bridged over a trench, (b) as-received AFM image profiles of one suspended NB under different load forces in contact mode, and (c) the normalized AFM image profile after removing the surface roughness by subtracting the image acquired at 106 nN from the data in (b). The force is also normalized in reference to the "zero setting point" of 106 nN (from Ref. 19).

An AFM system can be combined with a nano-indentation system and served as the imaging system to visualize the nano-object. The nano-indenter tip can be used as the "AFM" tip first to locate and visualize the nano-object and then switch to be the nano-indenter to indent the nano-object. The advantage of this integration is that the AFM tip alone is "soft" due to the limitation of the stiffness and harness of the AFM tip. In addition, the AFM tip cannot be arranged to be perpendicular to the nanowire surface and derives slip and

friction during indentation between the sample surface and the AFM tip. The unified system of AFM and nano-indentation are more effective in finding the nano-object, achieving high loading, monitor the materials response at near-real time.

Nano-indentation hardness can be defined as the indentation load (force) divided by the resulted projected contact area of the indentation.[24] It is the average pressure that a material can support the punch. From the measured load versus displacement curve, the indentation hardness can be obtained at the peak load by the following way[24]:

$$H = \frac{P_{\max}}{A}, \tag{4}$$

where $P_{\max}$ is the force value of the peak load and A is the resulted projected contact area of the indentation tip. The nano-indentation elastic modulus can be calculated using the Oliver–Pharr data analysis procedure[26] by fitting the unloading curve to a power-law relation. On the basis of the relationships developed by Sneddon[27] for the indentation of a semi-space bulk by any punch, a geometry-independent relation involving contact stiffness, contact area, and elastic modulus can be summarized as follows:

$$S = \frac{dP}{dh} = \frac{1}{\sqrt{\pi}}\beta E_r \sqrt{A}, \tag{5}$$

where β is a constant that depends on the geometry of the indenter ($\beta = 1.034$ for a Berkovich indenter)[28] and E_r is the reduced elastic modulus which taken into consideration the fact that the elastic deformation occurs in both the sample and the indenter. E_r is given by[24]:

$$\frac{1}{E_r} = \frac{1-\nu^2}{E} + \frac{1-\nu_i^2}{E_i}, \tag{6}$$

where E and ν are the elastic modulus and Poisson's ratio for the sample and E_i and ν_i are the same for the indenter, respectively.

A typical example of applying this technique is to indent a silver nanowire.[24] The representative AFM images of a silver nanowire by nano-indentation are shown in Fig. 5.[24] The wire is about 4 μm long and 42 nm in diameter. A drop of solution containing the silver nanowires was directly scattered on the glass substrate. Instead of using SiO_2 deposition to hold the NWs/NTs,[6] it was demonstrated that the natural adhesion forces between

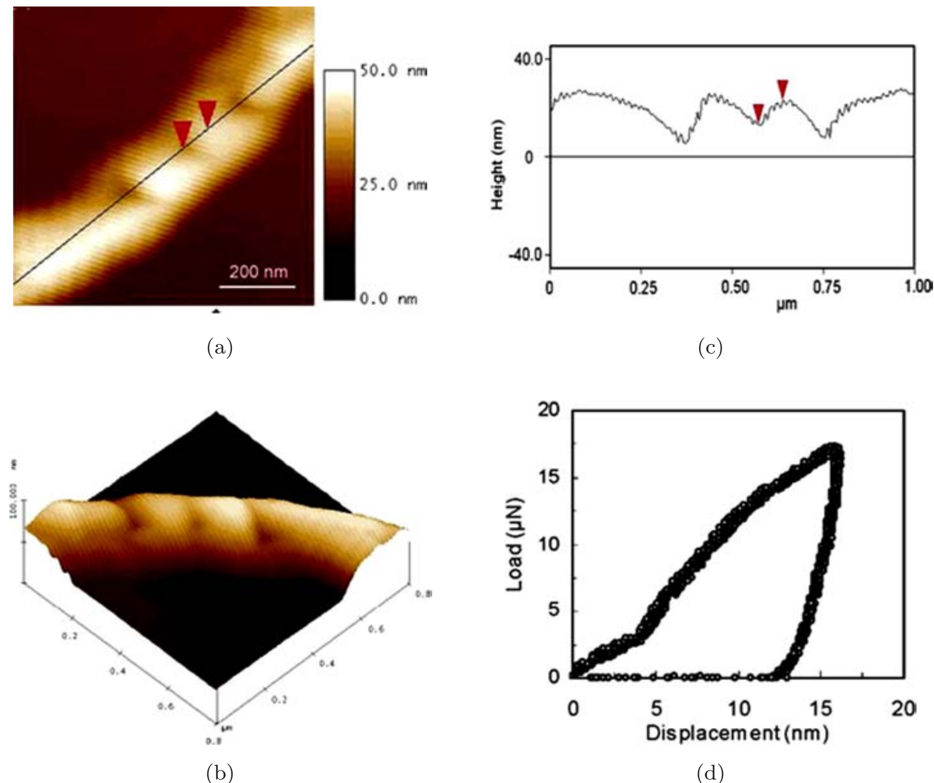

Fig. 5. (a) and (b) AFM images of indents on a silver nanowire. (c) Height profile of an indent on the wire and (d) a representative nano-indentation load-displacement curve (from Ref. 24).

the wires and the glass slide are strong enough to prevent the wire from moving/rolling on the glass slide and no any other means necessary to fix the nanowires on the substrate. The wires can be reproducibly imaged in contact mode of the AFM. In Ref. 24, a Berkovich diamond nano-indenter tip was used to image and locate a single nanowire and then *in situ* position the indent tip on the wire to perform an indentation test.

Some problems with nano-indentation would be the lack of a standard calibration method to deal with various problems like the indenter–tip roundness and the indentation size effect that are significant at the nanometer-scale. Some investigations tried to overcome these problems by various means. For example, Yang *et al.*[29] used nano-indentation to determine plastic deformation zone size at a fatigue crack tip, Shan and Sitaraman[30] have used nano-indentation in combination with finite element modeling to characterize mechanical (elastic and plastic) characters of the titanium thin films. Zhao *et al.*[31] proposed strain-gradient plasticity to interpret the indentation size effect.

3. Elastic Nanomechanics by *In Situ* Transmission and Scanning Electron Microscopy

TEM is a powerful tool for characterizing the atomic-scale structures of solid state materials with simultaneous information of chemical composition and electronic structures. A modern TEM is a versatile equipment that not only provide high spatial resolution imaging which can be easily better than 0.2 nm, but also give a quantitative chemical and electronic analysis from a region as small as 1 nm. A powerful and unique approach could be developed if we can integrate the structural information of a nanostructure provided by TEM with the mechanical property measured *in situ* from the same nanostructure.[32,33] Integrating with mechanical property measurement makes TEM to be a more powerful technique that not only can provide the mechanical properties of an individual nanotube but also can give the structure of the nanotube through electron imaging and diffraction, providing an ideal technique for understanding the property-microstructure correlations.[34] In the area in which the specimen was loaded in a conventional TEM, an electromechanical system can be built that allows not only the lateral movement of the tip, but also applying a voltage across the nanotube with the counter electrode. This set up is similar to the integration of a scanning probe technique with TEM. The static and dynamic properties of the nanotubes can be obtained by applying a controllable static and alternating electric field.

If an applied voltage is an alternating voltage, the charge on the tip of the nanotube is also oscillating, so is the force. If the applied frequency matches the natural resonance frequency of the nanotube, mechanical resonance is induced. By tuning the applied frequency, the first and the second harmonic resonances can be observed (Fig. 6). The analysis of the information provided by the resonance experiments relies on the theoretical model for the system. The most established theory for modeling mechanical system is the continuous elasticity theory, which is valid for large size object. For

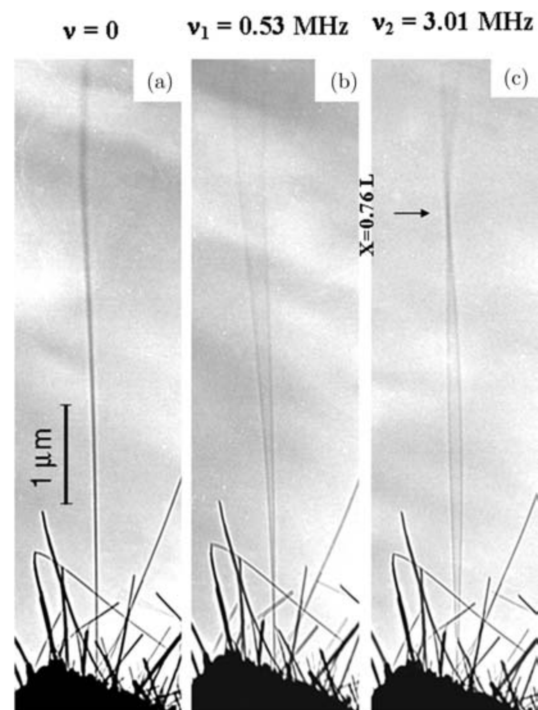

Fig. 6. Nanotube response to resonant alternating applied potentials. (a) In the absence of a potential, the nanotube tip ($L = 6.25$ mm, $D = 14.5$ nm) vibrated slightly because of thermal effects. Although thermal amplitude is difficult to evaluate, it was nevertheless used to measure the Young's modulus in a previous study. (b) Resonant excitation of the fundamental mode of vibration ($\nu_1 = 530$ kHz); the shape corresponds closely to that expected for a cantilevered uniform beam. The high contrast at the extremes of the oscillations is caused by the relatively long times spent at the turning points [compare with (a)]. (c) Resonant excitation of the second harmonic ($\nu_2 = 3.01$ MHz). Both the frequency and the shape correspond reasonably well to that expected for this harmonic. For this nanotube, $E_b = 0.21$ TPa (from Ref. 32).

atomic scale mechanics, we may have to rely on molecular dynamics. The diameter of the nanotube is between the continuous model and the atomistic model, thus, we need to examine the validity of applying the classical elasticity theory for the data analysis.

We have compared the following three characteristics between the results predicted by the elasticity theory and the experimental results shown in Fig. 6. First, the theoretical node for the second harmonic resonance occurs at 0.8L, and the experiment showed ~ 0.76L. Secondly, the frequency ratio between the second to the first mode is $\nu_2/\nu_1 = 6.27$ theoretically, while the observed one is $\nu_2/\nu_1 = 5.7$. The agreement is reasonably well if one looks into the assumptions made in the theoretical model: the nanotube is a uniform and homogeneous beam, and the root of the clamping side is rigid. The latter, however, may not be realistic in practical experiment. Finally, the shape of the nanotube during resonance has been compared quantitatively with the shape calculated by the elasticity theory, and the agreement is excellent. Therefore, we still can use the elasticity theory for the data analysis.

If the nanotube is approximated as a uniform solid bar with one end fixed on a substrate, from classical elasticity theory, the resonance frequency is given by[35]:

$$v_i = \frac{\beta_i^2}{8\pi}\frac{1}{L^2}\sqrt{\frac{(D^2 + D_i^2)E_B}{\rho}}\,, \tag{7}$$

where D is the tube outer diameter, D_i inner diameter, L the length, ρ the density, and E_B the bending modulus. The resonance frequency is nanotube selective and it is a specific number for a nanotube.

After a systematic study of the multi-walled carbon nanotubes, the bending modulus of nanotubes was measured as a function of their diameters (Fig. 7). The bending modulus is as high as 1.2 TPa (as strong as diamond) for nanotubes with diameters smaller than 8 nm, and it drops to as low as 0.2 TPa for those with diameters larger than 30 nm. A decrease in bending modulus as the increase of the tube diameter is attributed to the wrinkling effect of the wall of the nanotube during small bending.

A similar strategy can be applied in a scanning electron microscope. With careful design, the spacious room of SEM chamber makes the above technique easier to be applied in the SEM. As schematically shown in Fig. 8,[36] an electron-static excitation source can be fabricated and installed in a SEM chamber. The pizeo-driven stage allows accurate movement of the electron-static excitation source along the mutual-orthogonal axes X, Y and Z. A typical application example was applied to measure the elastic Young's modulus of ZnO nanowires and a dramatic increase of the modulus

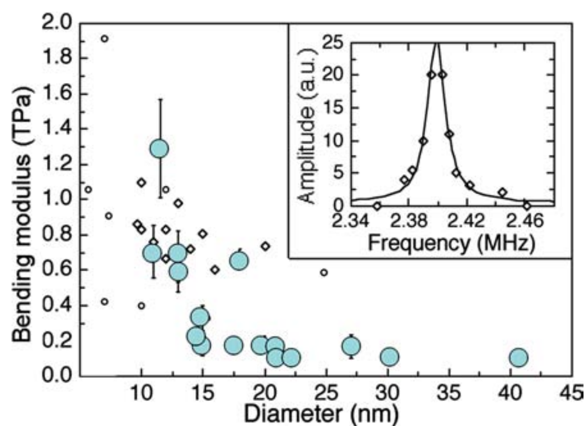

Fig. 7. Elastic properties of nanotubes. E_b as a function of diameter: solid circles, present data; diamonds, data from Ref. 16; open circles, data from Ref. 6. [A further data point at $D = 32.9$ nm and $E_b = 1.26$ TPa from Ref. 4 is obscured by the inset.] Error bars indicate absolute error in L and D; the error in the resonant frequency is negligible. The dramatic drop in E_b for $D \sim 12$ nm is attributed to the onset of a wave-like distortion, which appears to be the energetically favorable bending mode for thicker nanotubes. There is no remarkable change in the Lorentzian line shape of the resonance (inset) for tubes that have large or small moduli, although the low-modulus nanotubes appear to be more damped than the high modulus tubes (from Ref. 32).

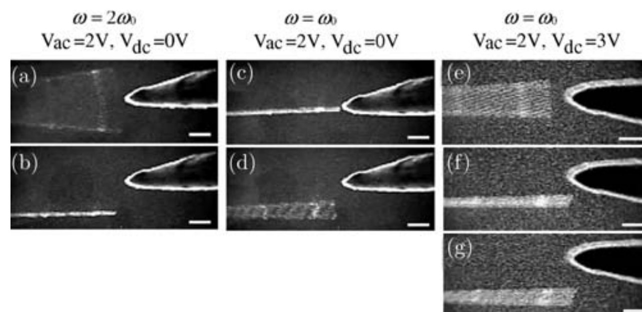

Fig. 8. Selected frames of a video recording the frequency responses of a NW subjected to (a), (c), (e) axial excitation, and (b), (d), (g) transverse excitation, showing: parametric resonance of (a) first order at $\omega = 2\omega_0$ and (e) second order at $\omega = \omega_0$ under axial excitation (the second order require a much higher dc voltage of 3 V); forced resonance (d) and (g) occurred at $\omega = 2\omega_0$ under transverse excitation; (f) transition from parametric to forced vibration. Scale bars represent 1 μm (from Ref. 36).

value with reducing the nanowire's diameter was discovered.[36]

The very sharp tungsten probes with typical tip radii ranging between 20–100 nm were fabricated.[37] The tips have to be very sharp to distinguish the two types of resonance for the subsequent experiments. The experiments[36] demonstrated that the occurrence of parametric resonance is determined by the relative orientation of the NW to the countering tip, and in fact by the direction of the force applied to the NW. As shown in Figure 8, if the NW is aligned (arranged in a line) with the tip, it will result in an axially applied force, parametric excitation can dominate. On the other hand, if the excitation source was applied transversely to the NW as shown in Figs. 8(b), 8(d), 8(f) and 8(g), a forced excitation would control. This is consistent with the parametric resonance of a macroscopic beam under periodic axial load, which is a typical subject of parametric instability.[38]

4. Plastic Nanomechanics by AFM−Ultra-High Strength of Nanowires/Tubes Measured by AFM

Measuring the strength of a carbon nanotube is a real challenge because it is too small to be clamped, thus, restricting the application of the conventional strength measurement technique. A novel experiment has been designed by Yu *et al.*,[3] who used double AFM tip to perform the tensile load, as shown in Fig. 9. The tensile strengths of individual MWNTs were measured with a "nanostressing stage" located within a scanning electron microscope. The tensile-loading experiment was prepared and observed entirely within the microscope and was recorded on video. The applied force is measured by the AFM tip, and the stretching distance is measured from the SEM image. The MWNTs broke in the outermost layer ("sword-in-sheath" failure), and the tensile strength of this layer ranged from 11 to 63 GPa. Analysis of the stress–strain curves for individual MWNTs indicated that the Young's modulus E of the outermost layer varied from 270 to 950 GPa. Transmission electron microscopy examination of the broken nanotube fragments revealed a variety of structures, such as a nanotube ribbon, a wave pattern, and partial radial collapse.

An AFM-based lateral loading has been applied to measure the Young's modulus E, yield strength, plastic deformation and failure of Au NWs.[10] The method involves AFM lateral manipulation of nanowires that are mechanically fixed to and positioned over trenches on a substrate (see Fig. 10). Challengingly, the AFM tip can be swept following a programmed manipulation path horizontally in the XY plane with trenches below the positioned NWs. The axis of the cantilever was aligned to be parallel to the nanowire as shown in Fig. 10. The AFM tip needs to be positioned 100–300 nm below the X–Y plane of the substrate and the lateral deflection of the cantilever can be monitored during the manipulation of the tip using a four-quadrant photodiode and the corresponding F–d trace.[10] Before each manipulation, a tapping-mode image of

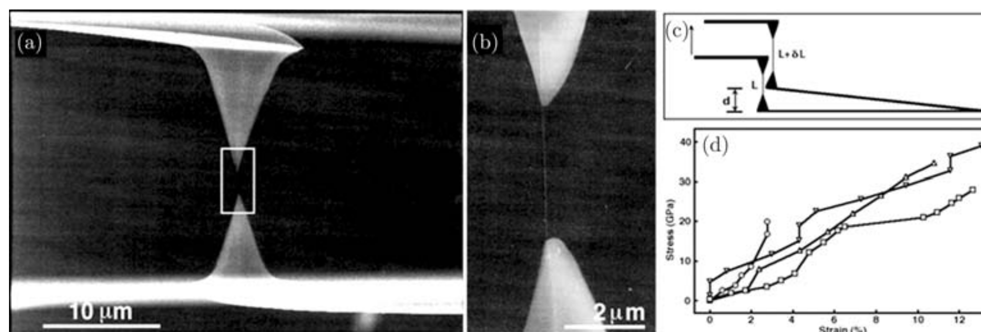

Fig. 9. (a) An SEM image of two AFM tips holding a MWCNT, which is attached at both ends on the AFM silicon tip surface by electron beam deposition of carbonaceous material. The lower AFM tip in the image is on a soft cantilever, the deflection of which is imaged to determine the applied force on the MWCNT. The top AFM tip is on a rigid cantilever that is driven upward to apply tensile load to the MWCNT. (b) High-magnification SEM image of the indicated region in (a), showing the MWCNT between the AFM tips. (c) Schematic showing the principle of the tensile-loading experiment. When the top cantilever is driven upward, the lower cantilever is bent upward by a distance d, while the nanotube is stretched from its initial length of L to $L + \delta L$ because of the force exerted on it by the AFM tips. The force is calculated as kd, where k is the force constant of the lower cantilever. The strain of the nanotube is $\delta L/L$. (d) Plot of stress versus strain curves for individual MWCNTs (from Ref. 3).

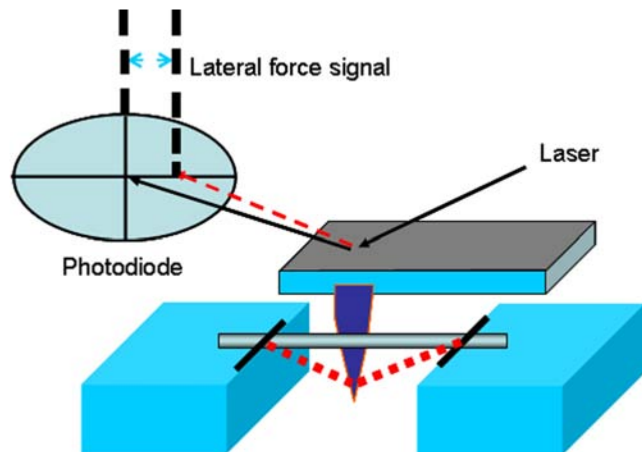

Fig. 10. Schematic of fixed wire in a lateral bending test with an AFM tip (from Ref. 10).

the suspended nanowire was recorded first. It was demonstrated that Au nanowire's yielding and plastic deformation properties are dramatically different from those of bulk nanometals with comparable grain size. Astonishingly, an ultra-high strength of Au NWs by almost 100 times of that of bulk materials was demonstrated. It was suggested that the constrained material volume and limited number of grains across the nanowire diameter preclude the elastoplasticity behavior reported in bulk nanometals. However, no direct dislocation controlled process was revealed at the nano- and atomic-scale. Detailed elastoplastic deformation mechanisms and the super strength need to be further proved by TEM or other imaging techniques. Future investigations on the atomic scale mechanisms of the superhigh strength of the Au NWs are necessary.

5. Plastic and Fracture Nanomechanics by *In Situ* Microscopy

Plastic deformation theories of bulk materials mainly focused on dislocation theories in single- and polycrystalline materials. The initiation and motilities of dislocations, the interaction activities among dislocations and the precipitates and grain boundaries as functions of temperature and strain rates determine most of the material's plastic properties in the bulk forms. For the nanopolycrystalline materials, it has been revealed that nanograin rotations,[39] dislocation-grain boundary reactions,[40] twin-formation and rotation etc. were active, and have special rules at nanoscale. However, for single-and/or poly-crystalline one-dimensional nanomaterials, the plastic-deformation mechanisms, particularly the dislocation controlled phenomena and mechanisms, are almost unknown. In this section, we introduce some recent developments in characterizing the nanowires plasticity and the plasticity-correlated dislocation activities by atomic scale *in situ* TEM observation.

5.1. *Tensile and bending experiments of individual nanowires in TEM*

An *in situ* transmission electron microscopy method was developed for conducting bending or axial tensile experiments for NWs and NTs in TEM and HREM.[7,8,41] The flexible operating conditions for easy tilting around the X and Y axes allow large angle tilting of the observed sample. This makes the measurement to be conducted at the area from where the atomic resolution TEM images can be recorded. A particularly-designed epoxy with desired strength can be carefully selected and make a colloidal thin film on the TEM grid. The thin films can be broken prior to or through TEM observation. Figure 11(a) shows a schematic illustration of the TEM grid with colloidal thin film covered. The nanowires were scattered on the TEM grid. The broken colloidal thin film can be curled or shrunk linearly under the heating/irradiation of the electron beam. The scattered NWs can then be curled into the colloidal thin films. Due to the complex

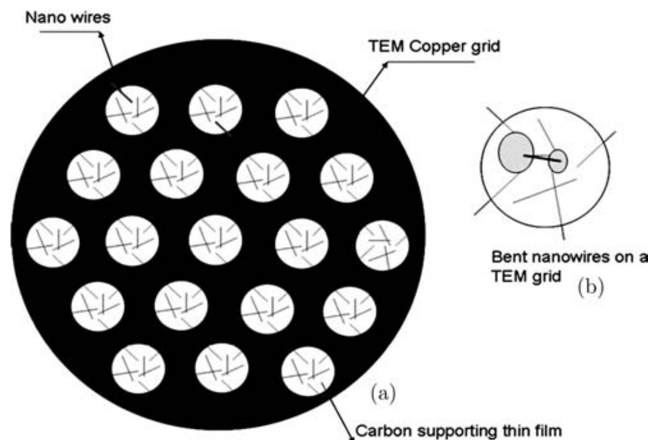

Fig. 11. (a) The NW bending test through heating/irradiating the carbon supporting film on a TEM Cu grid. The left shows the SiC NWs scattering on a TEM Cu grid and (b) shows a SiC NW (bold type) is bridged on two broken parts of the collodion supporting film. With the irradiation of the electron beam, the collodion thin film was curved, which eventually bent the SiC NWs (from Ref. 7).

geometry of the scattered nanowires on the TEM grid and the curl broken colloidal thin films, many NWs can be bent or being conducted axial tensile experiments. The advantage of this method is that no special TEM specimen holder was needed and no special mechanical tensile attachments were required. These advantages saved spacious space for titling the specimen along two orthogonal directions by large angles (± 30 degrees). Then, it provides the optional and ideal observing direction for *in situ* bending or axial tensile experiments on individual NWs.

The first successful example of using the recently developed method[41] to conduct the bending experiment on NWs was carried out for SiC NWs.[7] The SiC NWs were first dispersed on the specially designed TEM Cu grid covered with colloidal thin films. The colloidal thin films were broken prior to the TEM observation. An elastic, elastic–plastic transition and plastic deformation process was fully observed and recorded at the nano- and atomic-scale. Figure 12 shows an example of bending SiC NWs. A series of images of a single SiC NW which was deformed by the shrinking force created from the broken colloidal thin films on the TEM grid under the heating of electron beam were presented. The series of images captured *in situ* in both the elastic and plastic deformation modes can be viewed at Fig. 12. The strain rate was kept at a level of 10^{-4}–10^{-5}/s. The up limit strain for inducing elastic deformation of SiC NW is within the same order of magnitude as reported for *ex situ* studies,[42] and is consistent with theoretical prediction.[43]

Another example was conducted for Si NWs by axial tensile tests.[8] For the NWs with small Young's modulus and yield strength (1/5–1/10 of SiC), the axial tensile experiments on the NWs can be conducted *in situ* in TEM by the colloidal curl technique. Figures 13(a)–13(d) show a series of images of a single Si NW that was extended by the force created by the shrinkage of the broken colloidal thin film. A clear plastic deformation was observed at the center of the NW. Among the 9 Si NWs samples (ranging from 15 to 70 nm in diameter) having been studied, all of them had shown large elastic strain. The strain rate was kept at a level of $\sim 10^{-5}$/s. An as large as 426% diameter reduction (the ratio of incipient diameter over breakpoint's diameter (%)) and 125% elongation-rate were obtained at ambient temperature for a NW with an original diameter of 26 nm as shown in Figs. 13(a) through 13(d).

The more appealing function of the newly developed method[7,8,41] is that it allows *in situ* atomic-scale observation. In contrast to the conventional mechanical testing in TEM which usually could only conducts single tilt of the TEM specimen holder, the recent developed technique[7,8,41] allowed tilting the specimen along two orthogonal axes and observed the specimen along the low

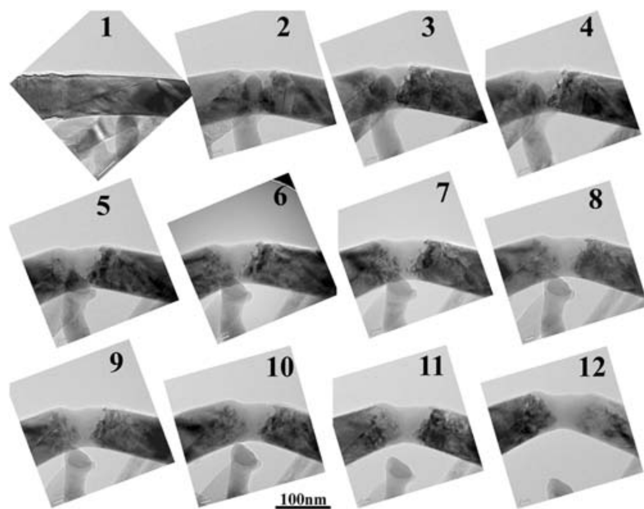

Fig. 12. A series of TEM images showing the bent SiC NWs from elastic (1) to plastic (2) and the large strain plasticity through 3 to 12. An amorphous character was directly observed in 3 and 12. The amorphous region shows transparent contrast in the middle which is distinctive with the crystalline regions (from Ref. 7).

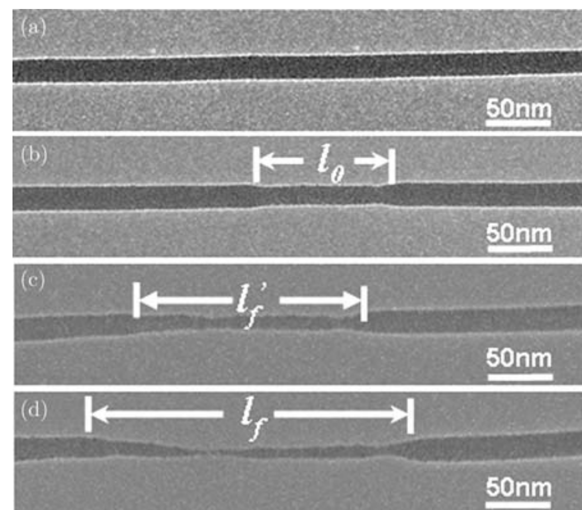

Fig. 13. (a)–(d) A Si NW during the *in situ* application of axial tension. The arrows indicate the corresponding positions of the extended nanowire throughout the procedure. The original diameter of the Si NW was 26 nm and after plastic elongation the diameter reduced to 6.1 nm (from Ref. 8).

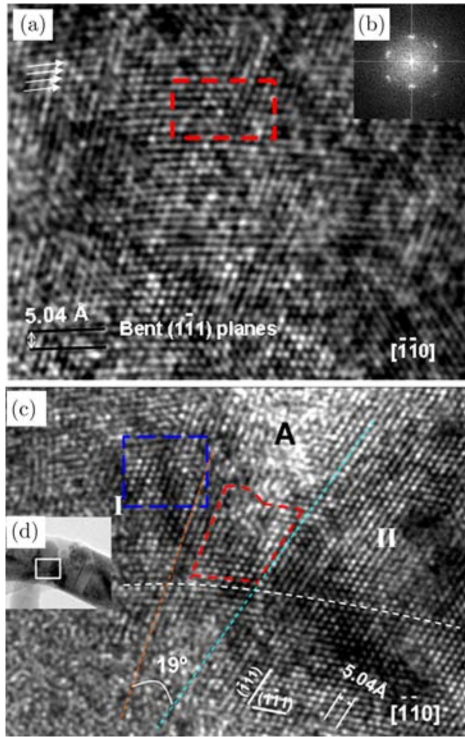

Fig. 14. An area at the middle stage of plastic bending of the bent SiC NW showing the features of lattice bending, formation of dislocations, and the process of amorphization. (a) An HREM image to show the initiation bending induced in-homogeneous plastic deformation of SiC NW. (b) shows a latterly recorded HREM image of the bent SiC NW showing the atomic scale features of the dislocation initiation, propagation and disordered structure. Character A indicates the amorphous region and I and II show the two tearing zones with dislocations around the tip (from Ref. 7).

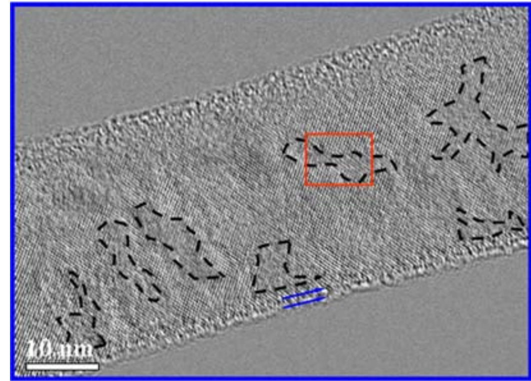

(a)

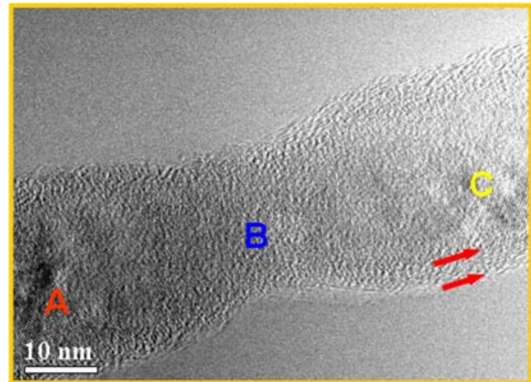

(b)

Fig. 15. *In situ* atomic-level high resolution electron microscopy study of an axially extended Si NW. (a) HRTEM image of the Si NW in a status of elastic–plastic transition and prior to severe plastic deformation. (b) The same Si NW after large-strain plastic deformation with a neck in the middle of the NW (from Ref. 8).

miller indices and have atomic-scale observations. Figure 14(a) shows the early stage of the elastic–plastic transition of the bent SiC NW that is characterized by homogeneous lattice distortion, dislocation nucleation and lattice relaxation in the compressed side. The elastic/plastic anisotropy is revealed in the incipient elastic–plastic transition period in the bent SiC NW when an external force is applied. The periodicity and continuity of the {111} family of lattice planes have been investigated. The stress can be continuously applied on the bent SiC NW and large plastic strain can be achieved. HREM images recorded later in the process reveal the atomic mechanisms of the plastic deformation features with large strains. Figure 14(b) shows a low magnification image at a later stage of the "tearing/fracturing" process.

For the case of axial tensile Si NWs, the plastic deformation mechanism of Si NW through *in situ* axial tensile experiment was revealed *in situ* at atomic scale in TEM as shown in Fig. 15. Figure 15(a) is an HREM image of the axial-extended Si NW at the initial elastic–plastic transition. Figure 15(b) is an HREM image of the extended Si NW at a later time.

In conjunction with TEM imaging, electron energy loss spectroscopy (EELS) can be applied to monitor the change in electronic structure of the NW during plastic deformation.[8] Figure 16[8] shows two sets of EELS spectra taken from the Si NW prior to and after super-plastic deformation of the Si NW. Using the scanning function, for each set of EELS analysis, 32 spectra were collected across the diameter of the Si NW. Seven of them were chosen to demonstrate that prior to and after the super-plastic deformation, the SiO_x surface layer did not diffuse radically into the inner layers of the Si NW, especially not at the largely strained area. Figure 16(a) is a series of EELS spectra taken from the Si NW prior to the initiation of plasticity.

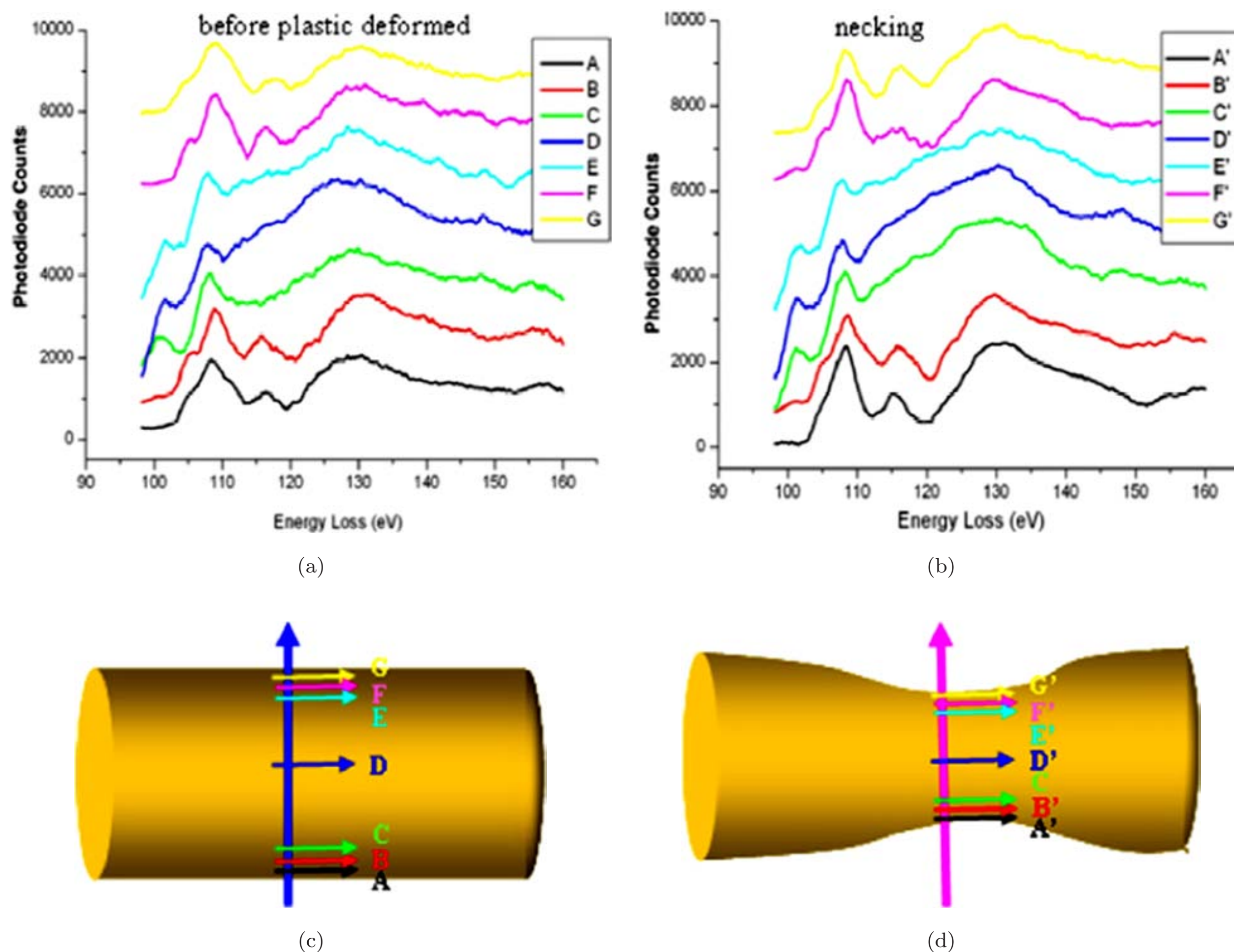

Fig. 16. Series of EELS line scans taken from a Si NW prior to and after large-strain plastic deformation. Both series of EELS spectra were taken across the NW width. (a) A series of spectra taken from the Si NW prior to plastic deformation. (b) A series corresponding to the NW with a super-plastic necking feature. (c) and (d) Schemes of the locations at which the spectra were taken for (a) and (b), respectively. The surface oxygen layer thickness was measured as the distance from the starting position A or A$'$ to the first peak position of oxygen in both oxygen spectra (from Ref. 8).

Figure 16(b) shows the corresponding series EELS spectra taken from the super-plastic deformed Si NW with the necking shape. The corresponding locations from where the EELS spectra were taken are indicated in Figs. 16(c) and 16(d).

5.2. *Other TEM correlated plastic deformations on one-dimensional nanomaterials*

Using the electron irradiation or heating can make the polymer thin films to shrink. As shown in Fig. 17, the deformed polymer thin films can bend carbon nanotubes and measure the strength of carbon nanotubes and the plastic deformation at the nanoscale.[44] A composite material was made by mixing the carbon nanotubes and epoxy.[44,45] Using ultracut microtome equipment, the dried mixture can be sliced to be thin films (70–100 nm) by diamond knife which are suitable for TEM observation. The successful example of this method was applied to measure the compressive strength of carbon nanotubes. The ultracut TEM slices (composites of epoxy and carbon nanotubes) were investigated by transmission electron microscopy (TEM) at 100 kV.[44] The TEM work was reported particularly difficult with the presence (and thickness) of the polymer, which strongly reduces the image contrast. Only those nanotubes that were close to or at the polymer surface were studied. The large amount of observations revealed that nanotubes collapsed under a compressive stress (revealed in Fig. 17, the buckling of the nanotubes in the compressive side) through a variety of deformation modes, depending mostly on the tube morphology and geometry. The compressive stress arises from polymerization shrinkage as well as from thermal effects associated

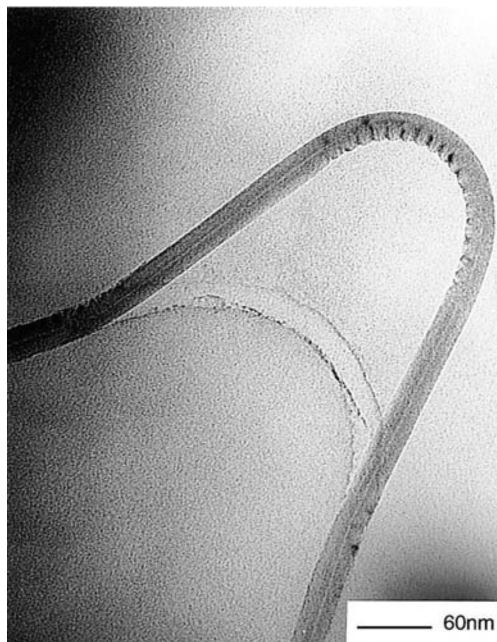

Fig. 17. Under high bending, nanotubes collapse to form kinks on the internal (compression) side of the bend (from Ref. 44).

with the electron beam in the TEM cell. The temperature increase could be significant but difficult to estimate. The room temperature curing epoxy used in research,[45] the measured linear contraction due to polymerization was only $(5.4 \pm 1.4)\%$. The behavior under stress of carbon nanotubes was found to strongly depend on the tube geometry and structure. The ultimate compressive strength was calculated from the mechanical properties of the epoxy and using a composite material's model. The compressive strength of carbon nanotubes was estimated to be about 60 GPa.

5.3. *TEM–STM integrated hybrid experiments for carbon nanotubes: Electro-mechanical integration*

There are growing interests in electro-mechanical coupling response of one-dimensional nanomaterials, for example, the giant-magnetic characters of Si nanowire under strain[14] and the strain-induced semi-conductance–conductance transitions of carbon nanotubes.[13] A TEM equipped with a pizeo-driven stage allows manipulating the specimen at nanometer scale.[46–54] With careful design, conducting electrodes can be also embedded in the pizeo-driven TEM holder. With sharpening the pizeo-driven tip, a STM system can be integrated inside a TEM. This makes it possible to simultaneously measure the electrical response (I–V curves) of one-dimensional nanomaterials under pizeo-driven displacement. The displacement can be measured either by the applied pizeo-driven voltage (nanoscale control of the X–Y–Z stage) or directly by the series time-resolved TEM images. More significantly, all powerful functions of TEM including the atomic-scale high resolution imaging, spatially resolved chemical composition analysis using EDS and EELS could be particularly conducted on the strained region being tested or positions at which the electrons are transported. Here we introduce a few successful examples to illustrate the set-up and functions of this type of technique. Initially, this technique was only applicable (or say mostly applied) to carbon nanotubes. Recently, it was successfully used in noncarbon tubes such as BN tubes.[48,51,52] Hopefully, in the future, it can be applied to other one-dimensional nanomaterials such as Si and ZnO nanowires and belts, etc.

Figure 18 is a schematic illustration of a TEM–SPM hybrid system in which a nanotube can be welded at the two ends of the two facing tips,[51] one is STM tip and the opposite side Au/Pt tip. Two ends or four ends electric feed through can be designed and carried out for the electrical conductance measurements. The current–voltage correlations with the strained nanotubes can be measured simultaneously with the TEM imaging and the

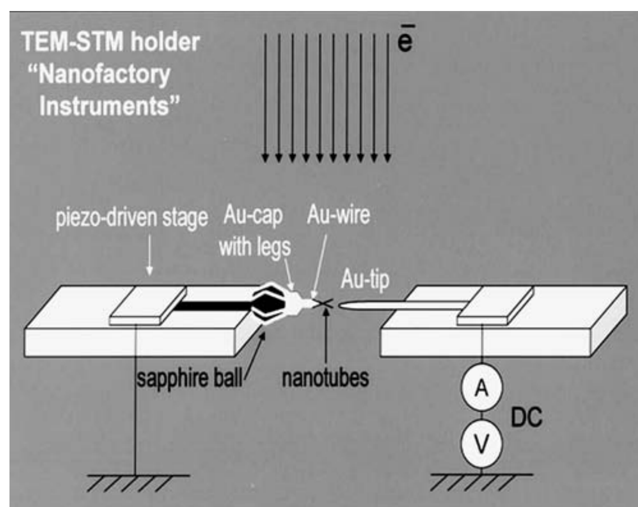

Fig. 18. Experimental setup for *in situ* electrical probing of nanotubes using a TEM–SPM hybrid specimen pizeo-driven holder, Nanofactory Instruments™ (from Ref. 51).

chemical composition analysis as well as the electronic state investigations. Both of tensile and compressive strains can be applied to the nanotubes. Currently, multiple electro-mechanical experiments have been successfully conducted for carbon nanotubes and BN tubes using the Nanofactory^{TM} TEM–SPM instrument.

A recent successful example[46,47] is shown in Fig. 19,[46] a MWNT was end-contacted and free standing inside a HRTEM which was integrated with a STM probe. With this set up, an atomic-scale imaging and four-point electrical conductance measurement could be carried out simultaneously. The contact between a STM probe (not shown) and the nanotube tip was made by the deposition of amorphous carbon using electron beam radiation. This type of irradiation-induced carbon is strong and conductive[54] and has no effects on the intrinsic conductance properties of the tested materials.[54] Interestingly, when applying a bias of about 2 V, the catalyst particle on the nanotube tip could be melted and moved rapidly toward the STM probe. The nanotube tip was broken after the catalyst particle passes through and made each wall of carbon nanotube being contacted by the amorphous carbon or the STM probe. On the other end of the nanotube, the multiple-walls of the nanotube were contacted to the carbon fiber.[47] The plastic deformation mechanism was revealed and a super-plastic feature was demonstrated for the carbon nanotubes when electric current was applied to pass through the tube. High temperature (around 2000°C derived from the electric current passing through the nanotube) was thought to contribute to the super-plastic deformation features of the carbon nanotubes and it was proved theoretically.[55] Through the pulling process of the carbon nanotube, the nanotubes penetrate from the outside layer to the inside layers which implied and confirmed the outside layer conduction mechanism of the multiple-wall carbon nanotubes.

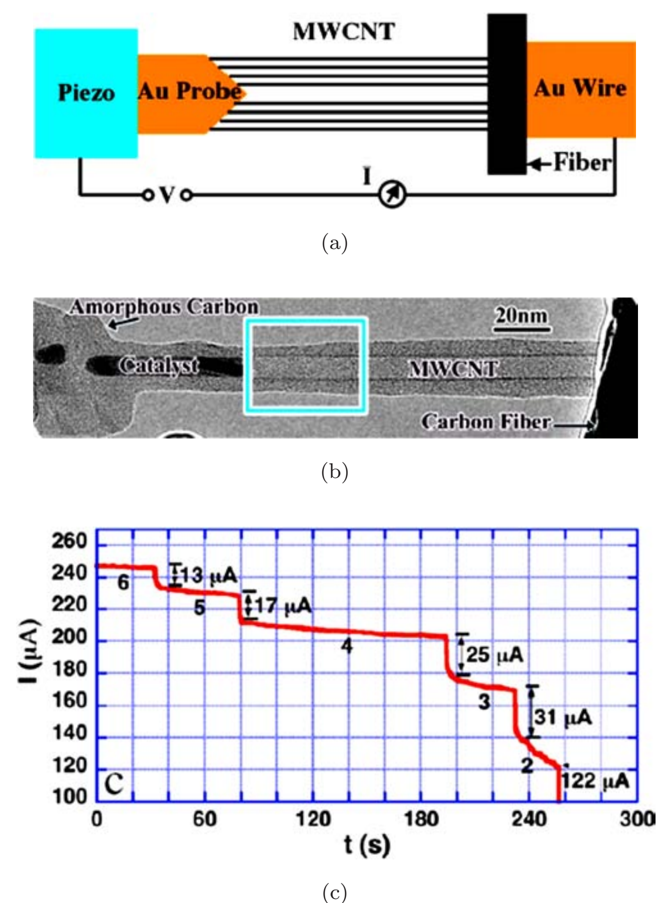

Fig. 19. (a) and (b) show that a MWNT grown on a carbon fiber was side-contacted by a STM probe, which is further attached to a piezomanipulator. The carbon fiber is glued to a gold wire. The MWNT in (b) has a catalyst particle on the tip. The frame in (b) indicates the location of the breakdown. (c) The current–time (I–t) curve of the breakdown of the MWNT (from Ref. 46).

A compressive stress could also be applied to the one-dimensional nanomaterials simultaneously with measuring the conducted electric signals. Several successful examples were demonstrated for carbon nanotubes and BN tubes.[48,51,52] A typical example is shown in Fig. 20 for the pizeo-electric effect of BN tubes by bending the BN tubes using the TEM–SPM method in a TEM chamber.[52] A sharp metallic STM Au/Pt tip was fixed on the movable end of a piezotube, facing its opposite electrode, i.e., another metal (Au, Pt or W) tip. A nanotube sample was first attached onto either an STM tip or its opposite counter tip/electrode. Then it was tightly fixed on the tip through manual manipulation with tweezers, and the position of the counter electrode can be adjusted to obtain an optimal gap between the metallic contacts in an optical microscope. Figures 20(a)–20(d) show the sequential images of a given BNNT bending and relief process inside a TEM. The bottom two HREM images show the released and compressive strained lattice images of the tested BNNT corresponding to the framed regions in (c) and (d), respectively. It clearly shows the wall lattice bending in (f) and became fully straight in (e). The electric-conductivity measurement revealed that the BN tube showed better conductivity under bending mode while kept an almost insulator behavior when strain was released. Similar to study,[7,8] the EDS and EELS investigations can

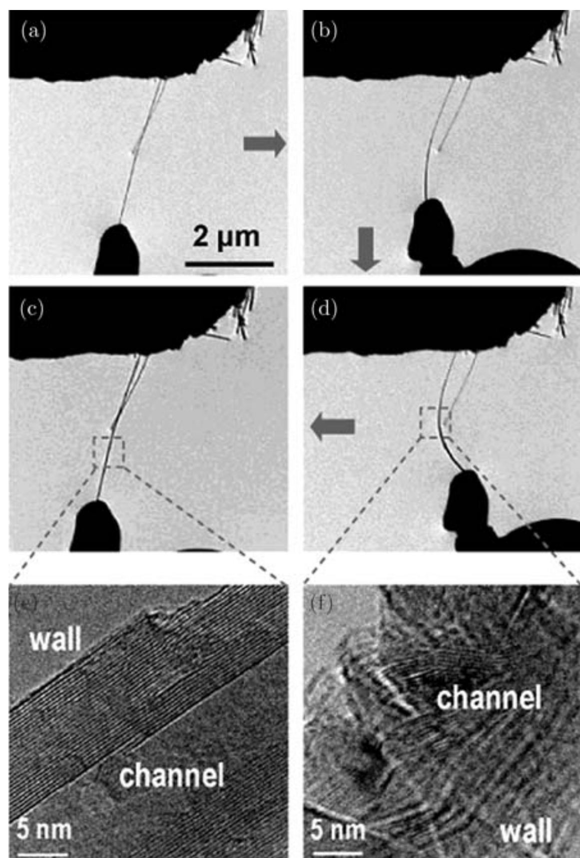

Fig. 20. (a)–(d). Sequential images of a given BNNT bending and relief process inside a TEM; the bottom two HREM images show the released and compressive strained lattice images of the tested BNNT corresponding to the framed regions in (c) and (d) respectively (from Ref. 52).

be conducted simultaneously with the high resolution imaging, straining and I–V measurments. Both of the EELS analysis and the HREM images show that not only lattices were bent elastically but also the electronic structure was changed under bending of the BN tube. A band gap shift was directly revealed in the EELS analysis which proved the theoretical predictions of the pizeo-electric effect of the BN carbon nanotubes.

Another example was successfully applied to bend a carbon nanotube and measure the electric conduction of the tube prior to and after the bending experiments.[54] The electron irradiation-induced contamination was used to fix the bent-tube to sustain the shape and keep the elastic strain. The contamination of the diamond-like carbon was demonstrated to be strong and conductive. No obvious conductance difference was revealed for the bent and undeformed carbon nanotubes. TEM–SPM system is a bit complicated system and so far, was only reported to work on the nanotube's in which the sharp Au tip can penetrate through the tube and be soldered. In the future, developments could be expected to expand to nanowires and nanobelts. The electro-mechanical measurements for one-dimensional nanomaterials can be also conducted in a scanning electron microscope and it has been successfully used in multiple examples.[56,57]

5.4. *TEM–AFM integrated hybrid system*

Force measurement is one of the major challenges for nanomechanics, particularly, with simultaneous high resolution imaging. However, with very careful design, this task could be quantified and executed in a high resolution transmission electron microscope together with an AFM cantilever. Recently, a dedicated AFM cantilever beam integrated with a single tilt TEM specimen holder for quantifying the nanoscale mechanics[48] was developed. An experimental setup is illustrated in Fig. 21 which used the commercialized Nanofactory Instruments AB^{TM} TEM–AFM hybrid specimen holder.[48] A silicon cantilever is attached to a fixed MEMS force sensor. An aluminum wire (for a subsequent calibration) with a mounted NW/NT sample was placed on the movable pizeo-driven side of the holder. Prior to the TEM observations, the relative positions between the nanowire and the cantilever can be manually adjusted under an optical microscope to obtain an optimal gap. Then, the nanoscale X, Y, and Z positions of the cantilever and each individual NW/NT were adjusted through the nanoscale pizeo-driven manipulation inside the TEM. The software automatically coordinates the stages to control the BNNT sample deformation strain as well as the deformation rate. The force measurement is

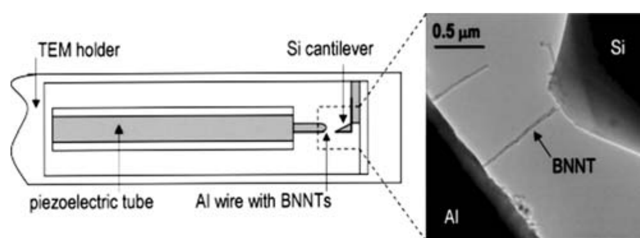

Fig. 21. Schematics of the experimental setup within an AFM–TEM holder; the inset on the right shows a TEM view of the framed area where an individual multi-walled BN nanotube stretches between a sample wire and a silicon cantilever. The position of the tube against the cantilever may be precisely adjusted through pizeo-driven displacements of the sample wire (from Ref. 48).

through the deflection of the Si cantilever. Prior to the key data measurements of BNNT bending forces, the force-displacement curves were recorded and were calibrated by means of indentation of the blank Al wire. The elastic and elasto-plastic deformation characters of a BN nanotube can be *in situ* investigated at nanoscale.

5.5. *Other methods*

Some concepts and *in situ* tensile techniques in conventional approach may also be borrowed to deform nano thin films by a special design and set up. Luckily, lattice images of the deformed materials in the polycrystalline system could also be acquired and recorded by a single-tilt TEM technique.[58,59] The deformation mechanisms of the polycrystalline materials, amorphous or single crystals could be investigated. This method with careful design has been applied to the one-dimensional nanomaterials[60] and could be expanded to other fields in the future.

5.6. *Super-plasticity of SiC NWs directly revealed by in situ axial tensile tests in SEM*

Due to the large available specimen manipulation space and versatile functions in SEM, it is the most widely used microscopy for various small scale measurements applied with an external field.[9,56,57,61–64] A bi-metallic extensor was designed for SEM to conduct axial tensile experiments on individual NWs.[9] Figure 22 shows the schematic illustration of the set up of the SEM NW tensile system (NTS). Following the structure and substructure determination of the SiC NWs, we conducted the *in situ* tensile tests inside a FEI Quanta 200 ESEM with our home-built nanotensile-testing stage. Two thermal bimetallic strips were mounted on the opposing position of the heating stage. The bimetallic strip is made of two materials with different thermal expansion coefficients. To achieve a significant deflection at lower operational temperature, the two materials must have a large mismatch in thermal expansion coefficients. The bimetallic strips were induced to bend by heating from a filament. The bimetallic strip was made of $Mn_{72}Ni_{10}Cu_{18}$ and Ni_{36} with the thermal expansion coefficients of 26×10^{-6} K^{-1} and 2.9×10^{-6} K^{-1}, respectively. The movable part of the bimetallic strips of a rectangle shape was 20 mm long, 3 mm wide and 0.25 mm in thickness.

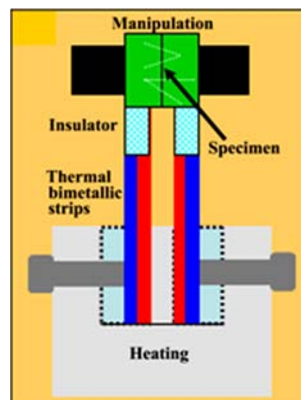

(a)

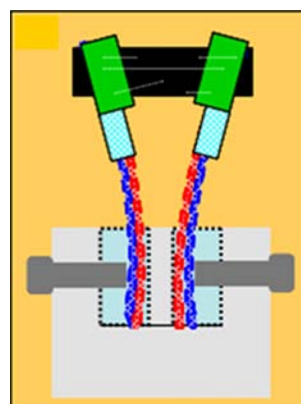

(b)

Fig. 22. (a) Schematic illustration of the tensile tool prior to extensile experiment with the SiC NWs scattered on the manipulator. (b) The conducting extensile experiment on the SiC NWs (top view) (from Ref. 9).

The bimetallic strip was operated below 150°C to avoid damage to testing sample. A significant deflection was clearly visible under the gentle heating conditions.

A successful example was first applied to the SiC NWs. The as-synthesized NWs were scattered between the two manipulators. Randomly distributed nanowires can be occasionally bridged across the two manipulators. The SiC NWs are long and straight and they tangled and bridged across the two manipulators. Two means were used to tightly "hold" the NWs on the manipulators. One is the friction force among the NWs (this force is very big due to the tangling features of the long SiC NWs), the other is "soldering" using the electron beam to create "contamination" points on the contact locations of NWs/manipulators. Combining these two methods, the manipulators can hold the NWs tightly without NW's slipping during tensile

experiments. By heating the bimetallic strips, the manipulators were then gradually moved away. A continuously increased temperature (up to 80°C) drove the manipulator so that a tensile load was applied to extend the clamped nanowire until fracture occurred. One point worthwhile to mention is that the manipulators were continuously to be driven to move away and the "soldered" SiC NWs were gradually to be flattened (zero strain), then elastically extended with large strain and lately plastically deformed, and finally fractured.

Eight single SiC NWs were pulled by the bimetallic extensor and the entire process was recorded *in situ* by SEM imaging. All of the NWs showed extremely large tensile strain (with an average fracture strain $\geq 25\%$) and plastic deformation characters. Figures 23(a)–23(d) demonstrate a representative experiment in which a SiC NW was

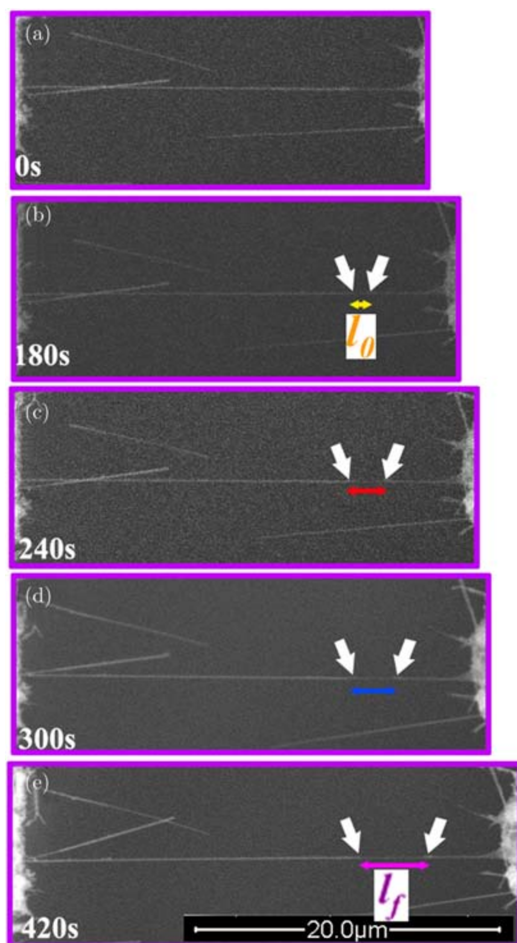

Fig. 23. The series images of an extended SiC NW in a SEM. (a) is the image of the SiC NW prior to axial extensile experiment and (b) through (e) are with the axial tensile load loaded. The white arrows indicate the corresponding extended locations of the SiC NW (from Ref. 9).

suspended and clamped between the two bimetallic actuating manipulators. The manipulators were used to gently pull the SiC NW to increase the strain with increasing temperature from 30° to 80°. The strain rate was estimated to be about 5×10^{-4} which is the same order as in study.[7] A 25 μm long, 96 nm diameter SiC NW was axially extended and finally broken in the middle. The resulting fragment attached on the left-hand had a length of at least 22 μm, whereas the fragment at the right-hand side had a length of at least 10 μm. Thus, the sum of the fragment lengths far exceeded the original section length. From the series images of Fig. 23, the total length of the SiC NW prior to the extensile experiment was measured to be $L = 25\,\mu$m, an elongation of $T = 7\,\mu$m was received after tensile testing. This derives an average elongation rate of $T/L = 28\%$. However, locally, as indicated by a set of paired arrowheads, the local elongation rate of the SiC NW exceeds 200%. The local elongation rate of the SiC NW is close to 220%, showing a super-plastic deformation strain.

6. Fracture of One-Dimensional Nanomaterials

The mechanical properties of one-dimensional nanomaterials include the elastic response and the Young's modulus determination, elastic–plastic transitions, extended plasticity and finally a broken feature. Some of the above-mentioned techniques are also applicable for investigating the fracture of the nanomaterials.

Using a double AFM tips to conduct the ultimate tensile experiment,[3] the plastic deformation and broken process of a carbon nanotube has been revealed (Fig. 24).

An *ex situ* experiment was carried out by putting the extensile broken carbon nanotube in HRTEM.[3] An interesting buckling character was revealed. Similar buckling features were also revealed in axial-tensile experiments for Si NWs as shown in Fig. 25 by the colloidal thin film shrinkage method.[7] Both of these experiments demonstrated plastic deformation features of the carbon nanotubes and Si nanowires. Using the TEM–STM combined technique, the ultimate extensile experiments have also been carried out for carbon nanotubes. A super-plasticity was demonstrated for carbon nanotubes with electric current fitting through the carbon nanotubes using the TEM–STM method as shown in Fig. 26.[47]

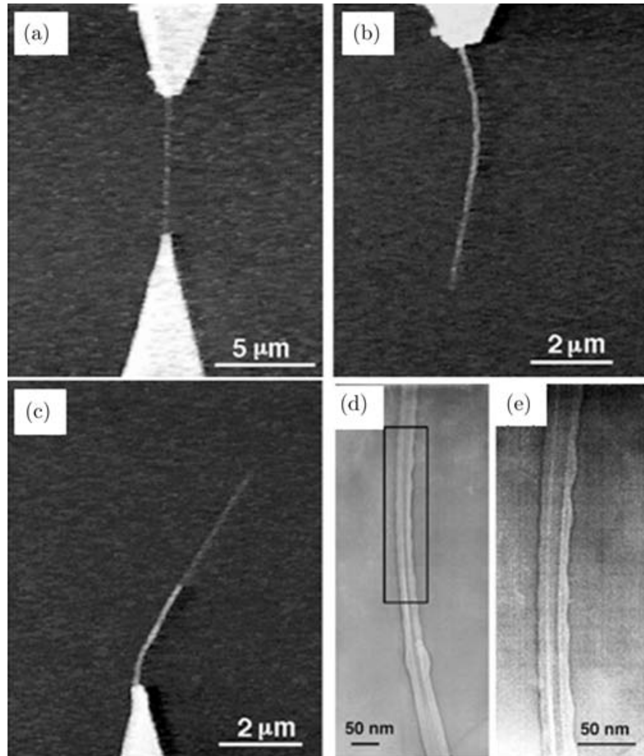

Fig. 24. Fracture of two individually loaded MWCNTs captured in two series of SEM images. The series shows (a) a MWCNT having a section length of ~6.9 mm under tensile load just before breaking. (b) After breaking, one fragment of the same MWCNT was attached on the upper AFM tip and had a length of ~6.6 mm. (c) The other fragment of the same MWCNT was attached on the lower AFM tip and had a length of ~5.9 mm. TEM images of fracture structures of several MWCNT fragments. (d) TEM image of a MWCNT (number 6) fragment having a wave pattern along the outer surface. (e) TEM image of the wave pattern of the same fragment at high magnification, corresponding to the indicated region in (d) (from Ref. 3).

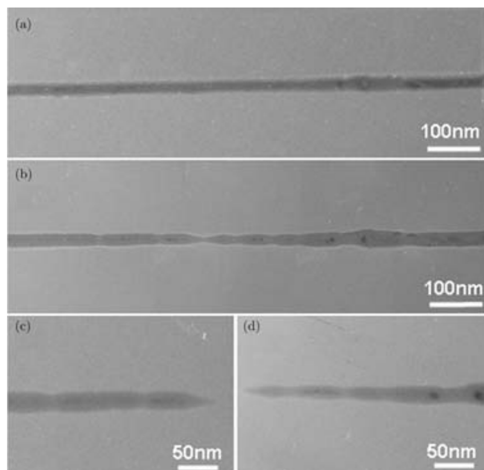

Fig. 25. (a) and (b) show the axial extended Si NW, and (c) and (d) show the characters of the broken Si NW and reveals the buckling characters (from Ref. 8).

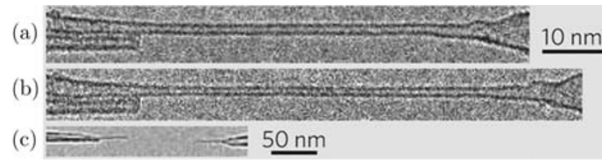

Fig. 26. (a)–(c) Tensile elongation of a SWCNT at room temperature without bias (images a and b are scaled to the same magnification). Initial length is 75 nm (a); length after elongation (b) and at the breaking point (c) is 84 nm, the low-magnification image of the SWCNT breaking in the middle (from Ref. 47).

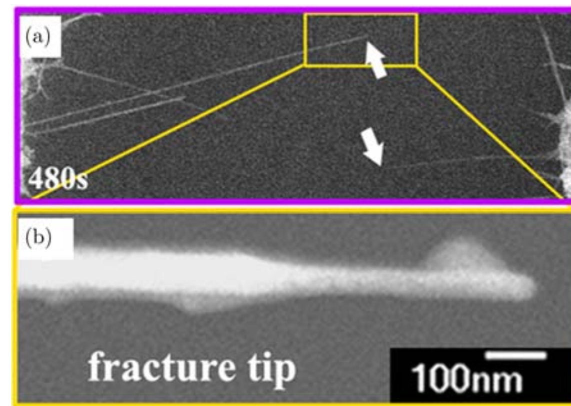

Fig. 27. A high magnification back scattering electron (BSD) image showing a broken tip of the SiC NW. A slender and uniform fracture tip was revealed and demonstrated a super-plastic feature as shown in (b) (from Ref. 9).

With a strong force applied to the axial tensile experiments, fracture can be easily achieved on nanowires or nanotubes using the method of bimetallic extensor.[9] As shown in Figs. 27(a) and 27(b), a uniform and super-plastic ductile fracture was revealed for SiC NWs in the *in situ* SEM tensile experiments. Interestingly, all of the above-mentioned experiments demonstrated that the co-valence bonded nanomaterials including carbon nanotubes,[3] Si nanowires[8] and SiC nanowires[7,9] are with ductile fracture characters at ambient temperature except for the super-plasticity[47] of carbon nanotubes whose super-plasticity was suggested to derive from a high temperature melting process.[46,47,55] A fracture feature was also revealed by AFM-nano-indentation combined technique for silver NWs as shown in Fig. 28.[24] The silver NW was cut by the diamond nano-indenter to be two pieces at ambient temperature. For the morphology as shown in Fig. 28, a ductile fracture character could be suggested. Some unpublished experiments demonstrated that the ionic-bonded materials with

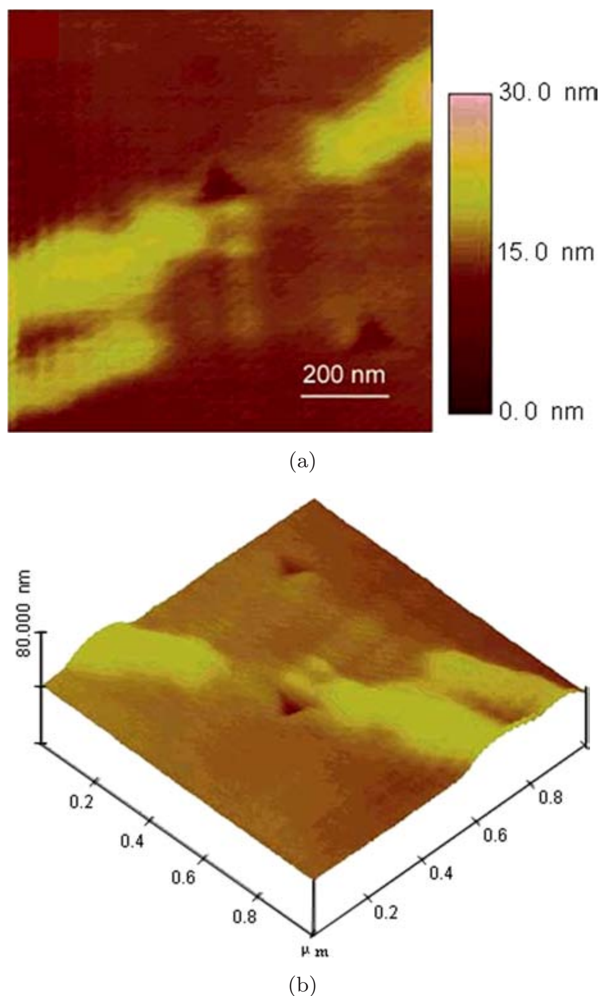

Fig. 28. AFM images of the cut silver nanowires by indentation impressions (a) 2D image and (b) 3D image (from Ref. 24).

a fast deformation rate showed brittle fracture features under both of bending and axial-extensile mode.[65]

7. Quantifying the High Resolution Stress and Strain for One-Dimensional Nanomaterials Mechanics

One of the fundamental approaches of nanomechanics on one-dimensional nanomaterials is the accurate force and displacement measurements at high resolution, for example at nanometer and nano-Newton-scale. However, the accurate force measurement at nanoscale is a big challenge for nanomechanics and particularly for one-dimensional nanostructure. The most difficult and challenging task is the direct and accurate force measurement due to the absent of commercialized nano-Newton-scale force sensors. People looked for alternative methods to evaluate and study the elastic and plastic strength of the one-dimensional nanomaterials. One approach was the thermally-activated[66,67] or the electric-field-forced vibration frequency measurements as introduced in Sec. 3. The limitation of these studies are that they are only applicable for elastic property measurements such as the elastic modulus and strength, and eventually, some complicated composite materials calculations have to be involved. In addition, one has to recognize what is the intrinsic vibration frequency. For the plastic deformation strength and force measurement, most of the investigations rely on the bent cantilevers in which the stiffness of a known material was particularly selected and shaped.[68–71] Using laser or other tracking techniques to monitor the bent beam, the force can be roughly calculated. It is one of the most applicable and popular methods used in many studies and commercialized products such as AFM and some hybrid systems of TEM–AFM.

In a parallel scenario, developing dedicated MEMS system could be one of the trends and solutions to measure the nano-Newton-force or developing nano-Newton-force sensors.[72–74] A nanomechanical test system (NMTS) was developed using the combed capacitors and thermal-activated actuators. As shown in Fig. 29(a), the combed capacitive system was used to measure the nano-Newton-force electronically and the thermal-activated actuators were used to measure the displacement. This NMTS system can be embedded in a single-tilt TEM specimen holder and allow the simultaneous high resolution imaging and the force-displacement measurement.[72,73] As shown in Fig. 29(b), the developed system has been successfully applied in conducting tensile experiments on carbon nanotubes[73] to obtain the force-displacement correlations. The obtained stress–strain curves and the Young's modulus as well as the strength of the tested materials were comparable to the values obtained by other methods. Some details regarding the nanocapacitor nanomechanics NEMS systems are available in Ref. 74.

The displacement measurement during the one-dimensional nanomaterials stress–strain test can be directly approached inside a SEM or a TEM by series frames of time-resolved imaging. With electron beam contamination soldering or other simple ways to prevent the one-dimensional nanomaterials from sliding, the strain measurement can be carried

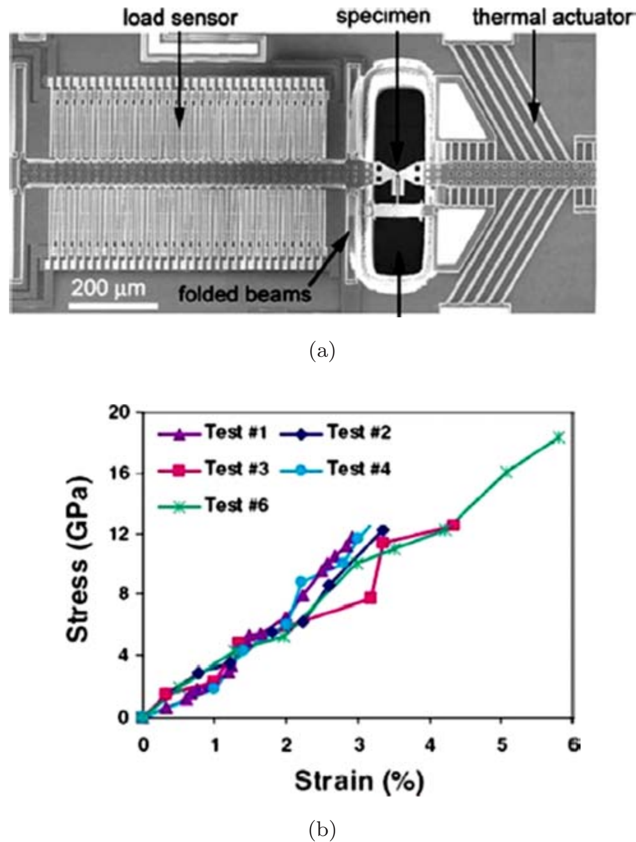

(a)

(b)

Fig. 29. The N-MTS system which includes thermal actuator, load capacitive sensor and specimen. Four-folded beams support the load sensor. (a) Testing device for *in situ* TEM, (b) stress–strain curves for the tested MWNTs (from Refs. 72 and 73).

out by simply recording a serial of time-resolved real images inside a SEM or TEM. When using a delicate pizeo-driven stage, the displacement can be directly read through driven the movement the pizeo-driven process. The big advantages of SEM- and TEM-based tensile/compressive techniques are that the full microstructure evolution process can be simultaneously revealed and recorded at the real time, for example, the dislocation initiation, propagation, and the failure mode of the one-dimensional nanomaterials. The FEG SEM can provide a resolution of 1–2 nm and a FEG TEM can provide an imaging spatial resolution at sub-nanometer level. The pizeo-driven stage can reach a resolution of nm scale in the X–Y plane and sub-nanometer scale along the Z direction.

8. Summary and Perspectives

With emerging applications of one-dimensional nanomaterials serving as building blocks of nanoelectronic devices, bendable and flexible electronic devices and the unusual mechanical properties of the one-dimensional nanomaterials,[75–82] the investigations on the mechanical properties and the related atomic scale mechanism are crucial in understanding their performance and novel applications. Due to the unique power of electron microscope in characterizing the atomic structure, electronic characters and the simultaneous imaging, the related techniques and methods in HREM and TEM are highly attractive and unique. With the improvement of measurement techniques, nanomechanics by electron microscopy and particularly, the related hybrid/integrated TEM/SPM, TEM/AFM, SEM/SPM, SEM/AFM etc. systems will be an important part of nanotechnology. As foreseen in the near future, we propose a few possible trends.

8.1. *Atomic scale imaging during in situ mechanical and electrical measurements*

Nanomechanics in TEM is a new emerging science for accurately evaluating the extraordinary mechanical properties of nanomaterials. Recently, some commercialized equipments/tools have been developed to conduct electric-current measurements, force measurements in the single-tilt TEM holder. A future direction can be to expand to the double-tiling TEM specimen holder to conduct the atomic-scale observation and direct correlate the mechanical and electrical signals when carrying out mechanical tests on single nano-objects.

8.2. *Quantitative multifunctional nanomeasurements at high spatial resolution*

With electrical field passing through a one-dimensional nanomaterial simultaneously with applying stress/strain fields have been conducted in a few experiments at nanoscale or high resolution electron microscopy, future perspectives will likely be in an area of TEM–STM combined method, which has the potential of measuring the local mechanical behavior induced electronic structure change.

8.3. *Atomic scale imaging of deformation process with simultaneous stress–strain plots*

One of the most important topics in nanomechanics regarding the strength theory would be

stress–strain correlations of the one-dimensional nanomaterials though it is very difficult to be accurately output. Nano-indentation and atomic force microscope as well as the related techniques and methods are powerful tools for this type of investigation. In the future, if high resolution electron microcopy imaging at atomic-scale could be integrated with the above techniques, it will give an outstanding opportunity to realize the deformation mechanisms of the one-dimensional nanomaterials. A bridge could be made between the plastic deformation theories and the strength theories for the one-dimensional nanomaterials, which is absent at this moment.

Acknowledgments

Z. Zhang and X. D. Han thank the support from Academic Human Resources Development in Institutions of Higher Learning under the Jurisdiction of Beijing Municipality, and the New Century Excellent Talents in University under the number of 05009015200701 and the Major State Basic Research Project of China under Grant No. 2007CB935400. Z. L. Wang thanks the support from US NSF and NASA. The authors thank the extensive editing help of Mr. Kun Zheng and Yuefei Zhang.

References

1. S. Iijima, *Nature* **354**, 561 (1991).
2. C. M. Lieber and Z. L. Wang, *MRS Bull.* **32**, 99 (2007).
3. M. F. Yu, O. Lourie, M. J. Dyer, K. Moloni, T. F. Kelly and R. S. Ruoff, *Science* **287**, 637 (2000).
4. M. M. J. Treacy, T. W. Ebbesen and J. M. Gibson, *Nature* **381**, 678 (1996).
5. S. Cuenot, S. D. Champagne and B. Nysten, *Phys. Rev. Lett.* **85**, 1690 (2000).
6. E. W. Wong, P. E. Sheehan and C. M. Lieber, *Science* **277**, 1971 (1997).
7. X. D. Han *et al.*, *Nano Lett.* **7**, 452 (2007).
8. X. D. Han *et al.*, *Adv. Mater.* **19**, 2112 (2007).
9. Y. F. Zhang *et al.*, *Adv. Funct. Mater.* (2007), in press.
10. B. Wu, A. Heidelberg and J. J. Boland, *Nat. Mater.* **5**, 525 (2005).
11. B. Wu, A. Heidelberg, J. J. Boland, X. M. Sun and Y. D. Li, *Nano Lett.* **6**, 468 (2006).
12. D. Tekleab, D. L. Carroll, G. G. Samsonidze and B. I. Yakobson, *Phys. Rev. B* **64**, 035419 (2001).
13. T. Cohen-Karni, L. Segev, O. Srur-Lavi, S. R. Cohen and E. Joselevich, *Nat. Nanotechnol.* **1**, 36 (2006).
14. R. R. He and P. D. Yang, *Nat. Nanotechnol.* **1**, 42 (2006).
15. P. B. Hirsch and S. G. Roberts, *Acta Mater.* **44**, 2361 (1996).
16. J. P. Salvetat, A. J. Kulik, J. M. Bonard, G. Andrew, D. Briggs, T. Stöckli, K. Méténier, S. Bonnamy, F. Béguin, N. A. Burnham and L. Forró, *Adv. Mater.* **11**, 161 (1999).
17. J. M. Gere and S. P. Timoshenko, *Mechanics of Materials* (PWS-KENT Press, Boston, 1990).
18. J. H. Song, X. D. Wang, E. Riedo and Z. L. Wang, *Nano Lett.* **5**, 1954 (2005).
19. W. J. Mai and Z. L. Wang, *Appl. Phys. Lett.* **89**, 073112 (2006).
20. V. Domnich, Y. Gogotsi and S. Dub, *Appl. Phys. Lett.* **76**, 2214 (2000).
21. S. Suresh, T. G. Nieh and B. W. Choi, *Script. Mater.* **41**, 951 (1999).
22. Y. Huang, W. D. Nie, R. Saha and Z. Xue, *J. Mech. Phys. Solids* **49**, 1997 (2001).
23. J. Knap and M. Ortiz, *Phys. Rev. Lett.* **90**, 226102-1 (2003).
24. X. D. Li, H. Gao, C. J. Murphy and K. K. Caswell, *Nano Lett.* **3**, 1495 (2003).
25. X. D. Li, X. N. Wang, Q. H. Xiong and P. C. Eklund, *Nano Lett.* **5**, 1982 (2005).
26. W. C. Oliver and G. M. Pharr, *J. Mater. Res.* **7**, 1564 (1992).
27. I. N. Sneddon, *Int. J. Eng. Sci.* **3**, 47 (1965).
28. G. M. Pharr, *Mater. Sci. Eng. A* **253**, 151 (1998).
29. F. Yang, A. Saxena and L. Riester, *Met. Mater. Trans. A* **29**, 3029 (1998).
30. Z. H. Shan and S. K. Sitaraman, *Thin Solid Films* **437**, 176 (2003).
31. M. H. Zhao, W. S. Slaughter, M. Li and S. X. Mao, *Acta Mater.* **51**, 4461 (2003).
32. P. Poncharal, Z. L. Wang, D. Ugarte and W. A. de Heer, *Science* **283**, 1513 (1999).
33. Z. L. Wang, P. Poncharal and W. A. De Heer, *Pure Appl. Chem.* **72**, 209 (2000).
34. Z. L. Wang, P. Poncharal and W. A. De Heer, *J. Phys. Chem. Solids* **61**, 1025 (2000).
35. L. Meirovich, *Elements of Vibration Analysis* (McGraw-Hill Press, New York, 1986).
36. C. Q. Chen, Y. Shi, Y. S. Zhang, J. Zhu and Y. J. Yan, *Phys. Rev. Lett.* **96**, 075505 (2006).
37. Y. S. Zhang, Y. J. Yan and J. Zhu, *J. Chin. Electron Microscopy Soc.* **23**, 483 (2004).
38. A. H. Nayfeh and D. T. Mook, *Nonlinear Oscillations* (Wiley Press, New York, 1979).
39. I. A. Ovid'ko, *Science* **295**, 2386 (2002).
40. H. Van Swygenhoven, *Science* **296**, 66 (2002).
41. X. D. Han, Y. F. Zhang and Z. Zhang, Chinese Patent: Application Number:200610057989.5.
42. X. D. Han, Y. F. Zhang, X. Q. Liu, Z. Zhang, Y. J. Hao and X. Y. Guo, *J. Appl. Phys.* **98**, 124307 (2005).

43. J. H. Wang, S. Yip, S. R. Phillpot and D. Wolf, *Phys. Rev. Lett.* **71**, 4182 (1993).
44. O. Lourie, D. M. Cox and H. D. Wagner, *Phys. Rev. Lett.* **81**, 1638 (1998).
45. H. D. Wagner, O. Lourie, Y. Feldman and R. Tenne, *Appl. Phys. Lett.* **72**, 188 (1997).
46. J. Y. Huang, S. Chen, S. H. Jo, Z. Wang, D. X. Han, G. Chen, M. S. Dresselhaus and Z. F. Ren, *Phys. Rev. Lett.* **94**, 236802 (2005).
47. J. Y. Huang *et al.*, *Nature* **439**, 281 (2006).
48. D. Golberg *et al.*, *Nano Lett.* **7**, 2146 (2007).
49. J. Cumings and A. Zettl, *Science* **289**, 602 (2000).
50. J. Cumings, P. G. Collins and A. Zettl, *Nature* **406**, 586 (2000).
51. D. Golberg, M. Mitome, K. Kurashima, C. Y. Zhi, C. C. Tang, Y. Bando and O. Lourie, *Appl. Phys. Lett.* **88**, 123101 (2006).
52. X. D. Bai, D. Golberg, Y. Bando, C. Y. Zhi, C. C. Tang, M. Mitome and K. Kurashima, *Nano Lett.* **7**, 632 (2007).
53. K. Suenaga *et al.*, *Nat. Nanotechnol.* **2**, 358 (2007).
54. M. Wang, L.-M. Peng, J. Wang and Q. Chen, *Adv. Funct. Mater.* **16**, 1462 (2006).
55. F. Ding, K. Jiao, M. Q. Wu and B. I. Yakobson, *Phys. Rev. Lett.* **98**, 075503 (2007).
56. C. H. Ke and H. D. Espinosa, *Appl. Phys. Lett.* **85**, 681 (2004).
57. C. H. Ke and H. D. Espinosa, *Small* **2**, 1484 (2006).
58. Z. W. Shan, J. M. K. Wiezorek, E. A. Stach, D. M. Follstaedt, J. A. Knapp and S. X. Mao, *Phys. Rev. Lett.* **98**, 095502 (2007).
59. Z. W. Shan, E. A. Stach, J. M. K. Wiezorek, J. A. Knapp, D. M. Follstaedt and S. X. Mao, *Science* **305**, 654 (2004).
60. H. Guo, P. F. Yan, Y. B. Wang, J. Tan, Z. F. Zhang, M. L. Sui and E. Ma, *Nat. Mater.* (2007), doi:10.1038/nmat1984.
61. C. H. Ke, N. Pugno, B. Peng and H. D. Espinosa *J. Mech. Phys. Solids* **53**, 1314 (2005).
62. S. C. Mao, X. D. Han, M. H. Wu and Z. Zhang, *J. Appl. Phys.* **101**, 103522 (2007).
63. J. F. Luo, S. C. Mao, X. D. Han, Z. Zhang, J. Wu and M. H. Wu, *J. Appl. Phys.* **102**, 043526 (2007).
64. Y. Zhu, F. Barthelat, P. E. Labossiere, N. Moldovan and H. D. Espinosa, *Proc. 2003 SEM Annual Conf. Exposition on Experimental and Applied Mechanics*, Session 77, Paper 155, Charlotte, North Carolina, 2–4 June 2003.
65. K. Zheng, Y. H. Yue, X. D. Han, Y. F. Zhang, Z. Zhang and Z. L. Wang, ZnO NWs room temperature brittleness under tensile and bending test (2007), unpublished work.
66. A. Krishnan, E. Dujardin, T. W. Ebbesen, P. N. Yianilos and M. M. J. Treacy, *Phys. Rev. B* **58**, 14013 (1998).
67. N. G. Chopra and A. Zettl, *Solid State Commun.* **105**, 297 (1998).
68. W. Z. Rong, W. Q. Ding, L. Maldler, R. S. Ruoff and S. K. Friedlander, *Nano Lett.* **6**, 2646 (2006).
69. S. N. Lu, Z. Y. Guo, W. Q. Ding and R. S. Ruoff, *Rev. Sci. Instrum.* **77**, 056103 (2006).
70. M. F. Yu *et al.*, *Nanotechnology* **10**, 244 (1999).
71. M. F. Yu, B. S. Files, S. Arepalli and R. S. Ruoff, *Phys. Rev. Lett.* **84**, 5552 (2000).
72. Y. Zhu and H. D. Espinosa, *Proc. Natl. Acad. Sci. USA* **102** 14503 (2005).
73. Y. Zhu, C. Ke and H. D. Espinosa, *Experimental Mech.* **47**, 7 (2007).
74. H. D. Espinosa, Y. Zhu and N. Moldovan, MEMS-based material testing system, *Encyclopedia of Materials: Science and Technology* (Elsevier Ltd., 2006), pp. 1–10.
75. C. Yang, Z. H. Zhong and C. M. Lieber, *Science* **310**, 1304 (2005).
76. H. O. Jacobs, A. R. Tao, A. Schwartz, D. H. Garcias and G. M. Whitesides, *Science* **296**, 323 (2002).
77. D. Y. Khang, H. Q. Jiang, Y. Huang and J. A. Rogers, *Science* **311**, 208 (2006).
78. A. J. Kulkarni, M. Zhou, K. Sarasamak and S. Limpijumnong, *Phys. Rev. Lett.* **97**, 105502 (2006).
79. P. X. Gao, Y. Ding, W. J. Mai, W. L. Hughes, C. S. Lao and Z. Wang, *Science* **309**, 1700 (2005).
80. A. J. Kulkarni and M. Zhou, *Acta Mech. Sinica* **22**, 217 (2006).
81. Z. L. Wang and J. H. Song, *Science* **312**, 242 (2006).
82. X. D. Wang, J. H. Song and Z. L. Wang, *Science* **316**, 102 (2007).